Journal of Structural Geology 32 (2010) 2022–2041

Contents lists available at ScienceDirect

Journal of Structural Geology

journal homepage: www.elsevier.com/locate/jsg

Three-dimensional characterization of a crustal-scale fault zone: The Pusteria and Sprechenstein fault system (Eastern Alps)

Andrea Bistacchi [a,*], Matteo Massironi [b], Luca Menegon [b,c]

[a] Dipartimento di Scienze Geologiche e Geotecnologie, Università degli Studi di Milano Bicocca, Piazza della Scienza 4, 20126 Milano, Italy
[b] Dipartimento di Geoscienze, Università degli Studi di Padova, Via Giotto 1, 35137 Padova, Italy
[c] Institutt for Geologi, Universitetet i Tromsø, Dramsveien 201, 9037 Tromsø, Norway

ARTICLE INFO

Article history:
Received 14 October 2009
Received in revised form
20 May 2010
Accepted 16 June 2010
Available online 23 June 2010

Keywords:
Fault zone architecture
3D modelling
Damage
Contractional jog
Cataclasite
Phyllonite

ABSTRACT

The characterization and representation of fault zones is of paramount importance for studies of fault and earthquake mechanics, since their rheological and geometric complexity controls seismic/aseismic behaviour and fluid circulation at depth. We present a 3D geological model of a fault system, created by integrating borehole and surface structural data, which allows us to bridge the gap between outcrop-scale descriptions and large-scale geophysical models. The model integrates (i) fault geometry and topology, (ii) fault-rock distribution, and (iii) characterization of fracturing in damage zones at the km scale. The dextral-reverse Pusteria and Sprechenstein-Mules Faults (Italian Eastern Alps) provide an opportunity to study fault rocks and damage distribution as a function of host-rock lithology and fabric, and of fault geometry. A first-order control is exerted by the composition of protoliths (quartzo-feldspathic vs. phyllosilicate-rich) and/or by the presence of an inherited anisotropic fabric (massive vs. foliated), resulting in a marked asymmetry of damage zones. Interestingly, the pervasive foliation typical of some protoliths may explain both this asymmetry and the relative weakness of one of the faults. The importance of geometrical factors is highlighted when the damage zone thickness increases five times in proximity to a km-scale contractional jog. On the other hand, the type of fault rock present within the fault core does not show a direct relationship with damage intensity. In addition, the thickness of damage zones along planar fault segments does not appear to grow indefinitely with displacement, as might be envisaged from some scaling laws. We interpret both of these observations as reflecting the maturity of these large-displacement faults.

1. Introduction and motivation

In recent years, a large number of papers have addressed the characterization of crustal-scale fault zone architecture, which can be reconstructed from detailed field and laboratory studies (e.g. Chester and Chester, 1998; Billi et al., 2003; Faulkner et al., 2003; Collettini and Holdsworth, 2004; Di Toro and Pennacchioni, 2005; Jefferies et al., 2006; Dor et al., 2006; Micarelli et al., 2006). All these contributions, following the pioneering work of Chester and Logan (1986) on the Punchbowl Fault, share a common approach, involving a detailed characterization, on the meso- to micro-scale (10^2–10^{-6} m) of exhumed fault zones, which are considered as representative analogs of active faults at seismogenic depth (5–15 km). One important result of these studies is the conclusion that deformation in fault zones develops through increasing levels of localization, and that this process leads to a characteristic architecture (e.g. Ben-Zion and Sammis, 2003), which is described with a specific nomenclature (Sibson, 1986; Chester et al., 1993; Caine et al., 1996). Damage zones are defined as large volumes (up to 1 km thick) at the margins of the fault zone, where fracturing is relatively intense and pervasive with respect to the regional background. Core zones typically refer to localized horizons (up to a few meters thick) of intense deformation, where much of the displacement is accumulated and fault rocks are developed. The term “core zone” is sometimes used in a broader or different sense. For instance, Faulkner et al. (2003) describe a 1 km thick fault core for the Carboneras Fault, comprising both fault rocks (phyllonites, cataclasites) and less deformed hectometric lozenge-shaped dolomite bodies (lithons), and Ben-Zion and Sammis (2003) show very effectively how this terminology is inherently scale-dependent.

In any case, most papers on fault zone architecture focus on characterization of exhumed core zones, fault rocks, and related

* Corresponding author.
E-mail address: andrea.bistacchi@unimib.it (A. Bistacchi).

0191-8141/$ – see front matter © 2010 Elsevier Ltd. All rights reserved.
doi:10.1016/j.jsg.2010.06.003

deformation processes (Chester and Chester, 1998; Faulkner et al., 2003; Di Toro and Pennacchioni, 2005; Jefferies et al., 2006; Collettini and Holdsworth, 2004). Other papers aim at characterizing exhumed damage zones on various scales (e.g. Sibson, 1986; Antonellini and Aydin, 1995; Vermilye and Scholz, 1998; Billi et al., 2003; Berg and Skar, 2005; Dor et al., 2006; Micarelli et al., 2006; Mitchell and Faulkner, 2009). A logical counterpart of this research is direct drilling of active fault zones at seismogenic depth, such as the San Andreas Fault Observatory at Depth (SAFOD), Nankai Trough and Chelungpu Fault drilling projects (www.icdp-online.org), which are providing data directly comparable to those from exhumed fault zones.

A 3D high-resolution model of exhumed fault zones at the km-scale, resulting from field observations and populated by structural and mechanical properties has never been given. Indeed fault zones have been mostly imaged in 3D on a larger scale with geophysical methods. 3D seismic surveys have been used extensively to reconstruct fault networks on the 10^4–10^3 m scale and, in tectonically active regions, it has been shown that core zones and damage zones can be imaged with head waves and trapped waves respectively (e.g. Li and Leary, 1990; Lewis et al., 2005, 2007), whilst "mean" fault surfaces can be reconstructed from the distribution of aftershocks (e.g. Carena and Suppe, 2002). Fracturing and physical property variations in damage zones can also be imaged by means of high-resolution seismic tomography (Martì et al., 2002; Francese et al., 2009), electrical resistivity (Ritter et al., 2005; Francese et al., 2009), and magnetotelluric methods (Unsworth et al., 1997; Ritter et al., 2005). Although these methods permit characterization of fault zones only indirectly, from remotely recorded physical properties, they are very important, because they investigate in 2D or 3D a volume comparable to that of the scale of large earthquakes (10^4 m).

This paper presents a model of the 3D architecture of two interacting crustal-scale fault zones, the Pusteria and Sprechenstein-Mules Faults (PF and SMF respectively), both belonging to the tectonic divide between the Alpine orogenic wedge and its South alpine hinterland (e.g. Schmid et al. 1989). The model is based on field and borehole data, the latter provided by BBT SE, in charge of the Brenner Basistunnel Project. The model volume is $10 \times 5 \times 1.5$ km, thus bridging the gap between classical outcrop-scale descriptions and geophysical models, and reaching the length scale of ruptures that characterize typical medium sized earthquakes. Vertical extension was obtained by means of two inclined boreholes (>2000 m of continuous cores and geophysical logs) and natural exposures in this mountainous area (almost 2000 m between the deepest valley and the highest peak). The model comprises the principal fault surfaces and the surrounding volume containing the damage zones. This paper presents and discusses structural features of the PF and SMF (fault-rock distribution, fracturing in damage zones, etc.), 3D modelling methodologies and strategies for representation of structural properties in 3D, and the results of this modelling for understanding the highly heterogeneous distribution of fracturing in damage zones and fault rocks in fault cores.

2. Geological setting

The Pusteria and Sprechenstein-Mules Faults (PF and SMF) belong to the Periadriatic system, the >600 km main tectonic divide between the Europe-vergent Alpine collisional wedge and the south-propagating Southern Alps fold-and-thrust belt (Schmid et al., 1989; Fig. 1). The collisional wedge is composed of the Adria-derived Austroalpine domain and the Penninic units of the Tauern window, including ophiolites and the underlying Europe-derived continental units (Bigi et al., 1990; Transalp Working Group, 2002). The Austroalpine–Penninic wedge underwent complex tectono-metamorphic evolution during the Alpine subduction-collision event, whereas the Southern Alps escaped Alpine metamorphism (Kurtz et al., 1998; Dal Piaz et al., 2003, and references therein).

The E-W sub-vertical PF represents the ca. 200 km long easternmost segment of the Periadriatic system and laterally juxtaposes the Austroalpine basement and Permo-Mesozoic covers (northern block) with the South Alpine Permian Bressanone (Brixen) Granite (southern block). The NW–SE trending SMF is characterized by an array of brittle dextral fault zones, interconnected by transpressional stepovers, linking the Brenner detachment to the PF. The eastern tip of the SMF is found in the Valles Valley, thus making the SMF trace about 20 km long.

During the Oligocene the Periadriatic Lineament was a preferential channel for the rise and crustal emplacement of magmas from mantle sources (post-collisional magmatism; Borsi et al., 1978; Barth et al., 1989; Müller et al., 2001). This magmatism is documented in the study area by the Mules tonalite, from hereafter simply called as the "Tonalitic Lamella", since it is a sheet-like body intruded along the Periadriatic Lineament itself. Hence, three distinct units were involved in PF and SMF deformation (Fig. 1): (i) the Bressanone Granite, (ii) the Tonalitic Lamella, and (iii) the Austroalpine basement and Permo-Triassic cover rocks occurring at the Mules syncline nucleus.

The Bressanone Granite is coarse-grained and isotropic, and consists of quartz, K-feldspar, plagioclase, and biotite. The Tonalitic Lamella is persistently characterized by sub-vertical to N-steeply-dipping magmatic foliation, subparallel to the PF. The foliation is marked by the alignment of hornblende phenocrystals (up to 0.5 cm long) and tabular crystals of plagioclase and polycrystalline aggregates of quartz, within a plagioclase + quartz + biotite matrix (Bistacchi et al., 2003). The Austroalpine paragneiss are composed of quartz + muscovite + biotite + plagioclase ± garnet. The paragneiss are interleaved by micaschists, mylonites and phyllonites where the Alpine greenschist-facies metamorphic re-equilibration was concentrated (chlorite and white mica grow on biotite and garnet sites; Baggio et al., 1969; Mancktelow et al., 2001; Bistacchi et al., 2003). Locally, biotite ± amphibole-bearing orthogneiss can be found. The Austroalpine metamorphic covers, which occur at the core of the Mules syncline, are composed of Permo-Eotriassic clastic and mainly carbonatic Triassic sequences (Baggio et al., 1969; Bistacchi et al., 2003).

A marked difference exists between the Southalpine Bressanone Granite, which never experienced temperatures exceeding 200–250 °C during deformation, and the Tonalitic Lamella and Austroalpine basement, which underwent progressive cooling from ≥450 °C to less than 100 °C during the Oligocene to Present activity of the Periadriatic Lineament, thus developing mylonitic fabrics in the higher temperatures range (Mancktelow et al., 2001). However, only brittle deformations are considered in this study. Mylonites developing at higher temperatures are considered only as protoliths of Austroalpine and Tonalitic Lamella brittle fault rocks.

3. Timing and kinematics of faulting

The timing and kinematics of faulting are well constrained by relationships with the Oligocene intrusives, which cut the Austroalpine–Penninic nappe-stack and are in turn deformed by the faults themselves. This means that the development of the structures described in this paper can be attributed to a precise interval in the exhumation path, thus allowing a good definition of the physical and environmental conditions of faulting. The Pusteria fault zone shows an initial ductile to brittle deformation phase on the Austroalpine basement and Tonalitic Lamella, characterized by

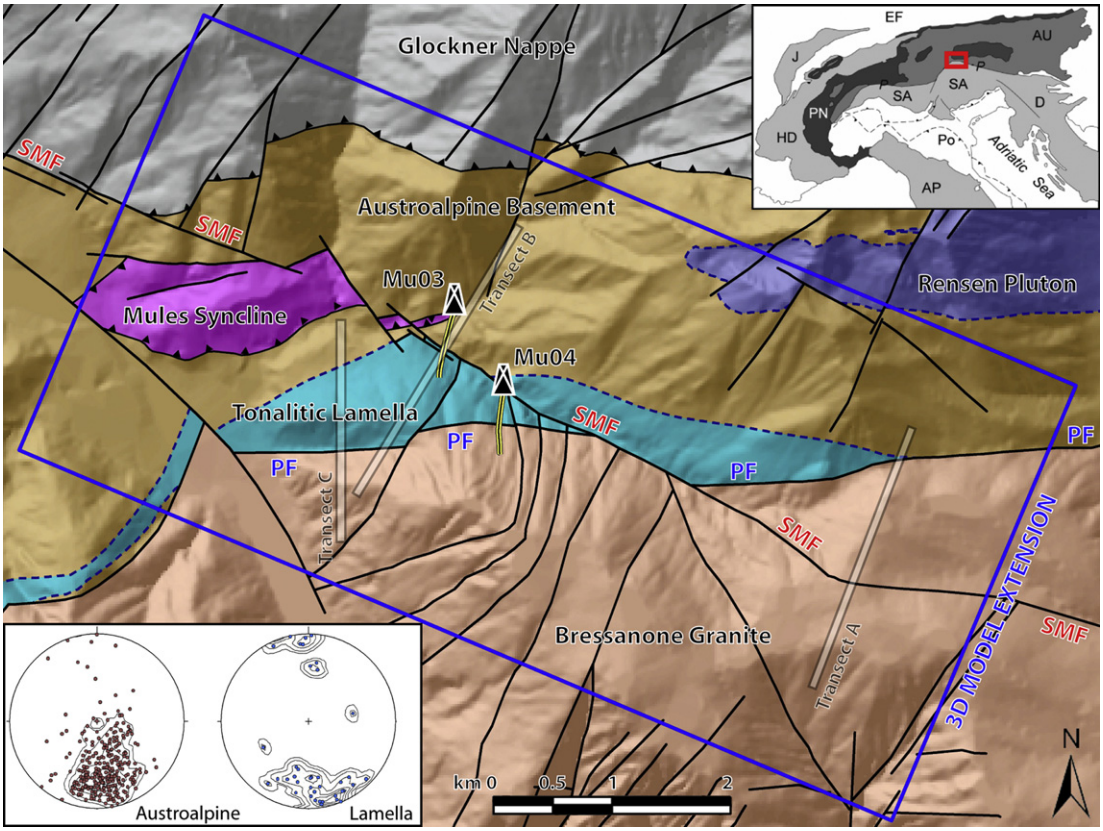

Fig. 1. Structural map of study area, with location of key transects and boreholes (horizontal projection of boreholes plunging to south shown in yellow). Stereoplots of ductile foliation in Austroalpine Basement and Tonalitic Lamella (contours at 1, 2, 4, 6, 8, 10%). Inset: location of study area (red box) within Alpine belt: EF = European foreland, J = Jura, HD = Helvetic-Dauphinois, PN = Penninic nappes, AU = Austroalpine domain, P=Periadriatic Lineament, SA = Southern Alps, D = Dinarides, Po=Po Plain, AP = Apennines. (For interpretation of the references to color in this figure legend, the reader is referred to the web version of this article.)

sinistral transtension along E-W trends, followed by a switch to dextral transpressional activity at 30 Ma (Mancktelow et al., 2001; Müller et al., 2001). Late dextral-reverse activity involved the whole Pusteria fault network (e.g. Schmid et al., 1997; Fodor et al., 1998) and is consistent with the NNW indentation of the Adria plate towards Europe, coeval, from the Early Miocene onwards, with tectonic unroofing of the Penninic units at the footwall of the Brenner detachment (Selverstone, 1988, 2005; Ratschbacher et al., 1991; Frisch et al., 2000).

The westernmost end of the PF is displaced by the NE-dipping SMF (Fig. 1), which was the kinematic linkage between the Periadriatic system and the extensional Brenner Detachment. Even if we cannot exclude that the activity of the PF and SMF slightly overlapped in time, we see no field evidence of the PF offsetting the SMF in the study area. The main phase of activity of the Brenner detachment is reported by Fügenschuh et al. (1997) at 20–13 Ma, which may be considered as a feasible time for this linkage to develop, and which is also confirmed by K-Ar ages from fault gouges of the SMF (14.5 ± 3.9 Ma, Zwingmann and Mancktelow, 2004). The fault zones and related brittle fault rocks described here are attributed to this time interval.

4. Methods

4.1. Structural analysis and mapping

Large-scale fault zone structure and brittle fault-rock assemblages of both the PF and SMF were reconstructed on the basis of detailed field work, inspection of continuous cores and geophysical logs from two inclined boreholes, which crosscut the fault zones almost perpendicularly, and microstructural observations. Detailed mapping on the 1:5000 scale was conducted in a 40 km^2 area covering the Mules and Isarco valleys, where the PF is dextrally displaced by the SMF (Fig. 1, and Supplementary 1). The boreholes (location in Fig. 1, logs in Supplementary 2 and Supplementary 3) cross the SMF at the boundary between the Austroalpine basement and the Tonalitic Lamella (borehole Mu03; Fig. 1) and the PF at the boundary between the Tonalitic Lamella and the Bressanone Granite (borehole Mu04; Fig. 1).

In this paper only features related to the younger brittle deformation phases are covered, whereas semi-brittle and ductile fault rocks, which occur in the Austroalpine and Tonalitic Lamella, will be considered as protoliths to brittle fault rocks. The Sibson (1977) classification, updated by Scholz (2002), is used throughout for fault rocks genetically related to the PF and SMF. In order to describe fault zone architecture, the fault core/damage zone concept is applied (Chester et al., 1993; Caine et al., 1996). This concept is inherently scale-dependent (Ben-Zion and Sammis, 2003) and, in this paper, the reference scale is that of the 3D model: 10^3 m. Hence, the term core zone will be used for relatively thin layers (5 -10 m thick) of mature fault rocks, generally developing along major tectonic boundaries and master faults, where much of the displacement took place. Damage zones refer to all other portions of the fault zone where deformation is more intense than in the country rocks, but little significant displacement occurred (on the reference scale).

4.2. Fracture density and classification of the degree of fault zone damage

Various structural parameters were systematically measured on outcrops in the damage zones, the most important being the number of fracture sets, fracture attitude, and spacing. In this analysis, we considered only fractures kinematically and geometrically related with SMF and PF (e.g. fractures that can be classified as R, R′,T,P, and possible rotations of R and R′, according to their attitude and kinematics; Petit, 1987). These data were regarded as the most suitable parameters for quantitatively characterizing the degree of damage. Supplementary 4 lists these and other data from ca. 1200 outcrops.

To measure fracture density in the field we calculated the "fracture density parameter" for selected outcrops in the damage zone of both the PF and SMF. This technique yields fracture density in terms of metres of fracture traces per unit area (Dershowitz and Herda, 1992; Dor et al., 2006). However, in order to populate the 3D model with the structural properties of the damage zone, classification of the rock mass consistent with the large scale (several km) and spatial resolution of the model (25 m per cell) was needed. A fundamental requirement of this classification is that it must be applied in the field according to macroscopic structural properties, and for this reason we developed the Damage Index (DI) classification method, which is presented in the following.

Fracture data from boreholes were derived from the interpretation of sonic borehole televiewer (BHTV) images, cross-checked with continuous cores (Supplementaries 2 and 3). These data are represented in terms of fracture density (number of fractures per unit borehole length), applying a correction for the angle formed by each fracture with the borehole axis.

Surveys of the Bressanone Granite and Tonalitic Lamella showed that the best proxy for damage in the fracturing-dominated distal damage zones is the number of fracture sets, a parameter easily assessable in the field and in boreholes. Approaching the fault core, fracturing becomes more intense and rotation of clasts more recurrent, until cataclastic deformation is dominated by comminution and shearing processes. Therefore, fracture spacing, block rotation, comminution and shearing must also be taken into account in the classification of rock masses which are very close to, or inside, the fault cores.

A peculiar type of evolution was observed in phyllonitic rocks, where brittle deformation preferentially produced cataclasite layers parallel to the pre-existing mica-rich foliation, whereas fracturing at high angles to the foliation was subordinate. In this case, the spacing between cataclasite seams is considered as a proxy for the degree of damage.

According to these observations, we introduce the Damage Index (DI) classification (Table 1), and show how it was applied and validated for the PF and SMF systems. A similar approach to rock mass classification is adopted in mining and tunnelling projects, in order to obtain rock mass strength estimates by means of semi-quantitative geological observations (e.g. Tzamos and Sofianos, 2007, and references therein), but it must be emphasized that only tectonic fractures are considered in the DI classification, and results of different classifications cannot be directly compared.

In this classification, the rock mass within an ideal fault zone is subdivided into 5 DI classes, according to increasing degrees of damage (Table 1). DI 1 refers to the regional background, and DI from 2 to 5 represent increasing levels of damage. The classification is conceived in a way such that DI 2 and 3 cover typical "distal" damage zones, and DI 4 and 5 cover "proximal" damage zones and core zones.

Table 1
The DI classification of rocks masses in a fault zone.

DI	Massive rocks	Phyllosilicate-rich foliated rocks	Occurrence in fault zones	Comparison with engineering geology and other classifications
1	Intact to interlocked undisturbed rock mass with a maximum of 3 persistent fracture sets.		Generally represents undisturbed rock occurring out of fault zones.	Analogous with "massive" and "blocky" classes in GSI[(2)]. Inclusive of first three classes ("intact", "low jointed", and "blocky") in TS[(3)].
2	Interlocked, partially undisturbed rock mass with 4 to 5 persistent fracture sets. At this level of fracturing, it is quite often possible to infer the kinematics of single fracture sets and to reconstruct their genetic relationship with the fault zone (R, R', T, P fractures[(1)]).		Generally characteristic of very distal damage zones.	Analogous with "very blocky" class in GSI[(2)] and in TS[(3)].
3	Disturbed rock mass with more than 5 persistent fracture sets. Fracture sets are distinct and well recognizable, only minor block rotations occur. Fractures can often be classified according to their kinematics and angle with respect to the fault zone (R, R', T, P fractures[(1)]).	Pervasive brittle reactivation of metamorphic foliations, with ca. 1-meter spacing of cataclasite seams.	Generally characteristic of distal damage zones.	May be compared with "blocky-disturbed" class in GSI[(2)] and in TS[(3)], although in these classifications nothing is mentioned about block rotation.
4	Rock mass with pervasive fracturing (fracture systems are no longer recognizable), and rotated blocks, grading to coarse fault breccias. Dominant deformation process is still fracturing, but block rotation is substantial and leads to a chaotic rock mass structure.	Pervasive brittle reactivation of metamorphic foliations, with dm- to cm-scale spacing of cataclasite seams.	Generally characteristic of proximal damage zones.	Related to "disintegrated" class in GSI[(2)] and in TS[(3)]. Vaguely resembles the definition of "kakirite" by Heitzmann (1985) and Bürgi et al. (1999). Includes "fault breccias" as defined by Dor et al. (2006) and "cataclastic breccias formed by crushing processes" as defined by Sibson (1986).
5	Fine-grained fault breccias, cataclasites, fault gouges and ultracataclasites, either non-foliated or foliated. These rocks derive from attrition process as defined by Sibson (1986) or from abrasive wear processes (e.g. Scholz, 2002), and are always characterized by comminution. Shearing can be dominant in foliated types.		Generally characteristic of fault cores and proximal damage zones, but thin localized volumes with DI 5 can be found also at some distance from master faults.	Analogous with "disintegrated" class in GSI[(2)] and in TS[(3)], "laminated sheared" class in Hoek et al. (1998), and "kakirite" by Heitzmann (1985).

[(1)] See Petit, 1987, for a classification of secondary fractures. [(2)] GSI: Geological Strength Index, by Hoek (1994) and Hoek and Brown (1997). [(3)] TS: rock mass classification in Tzamos and Sofianos (2007).

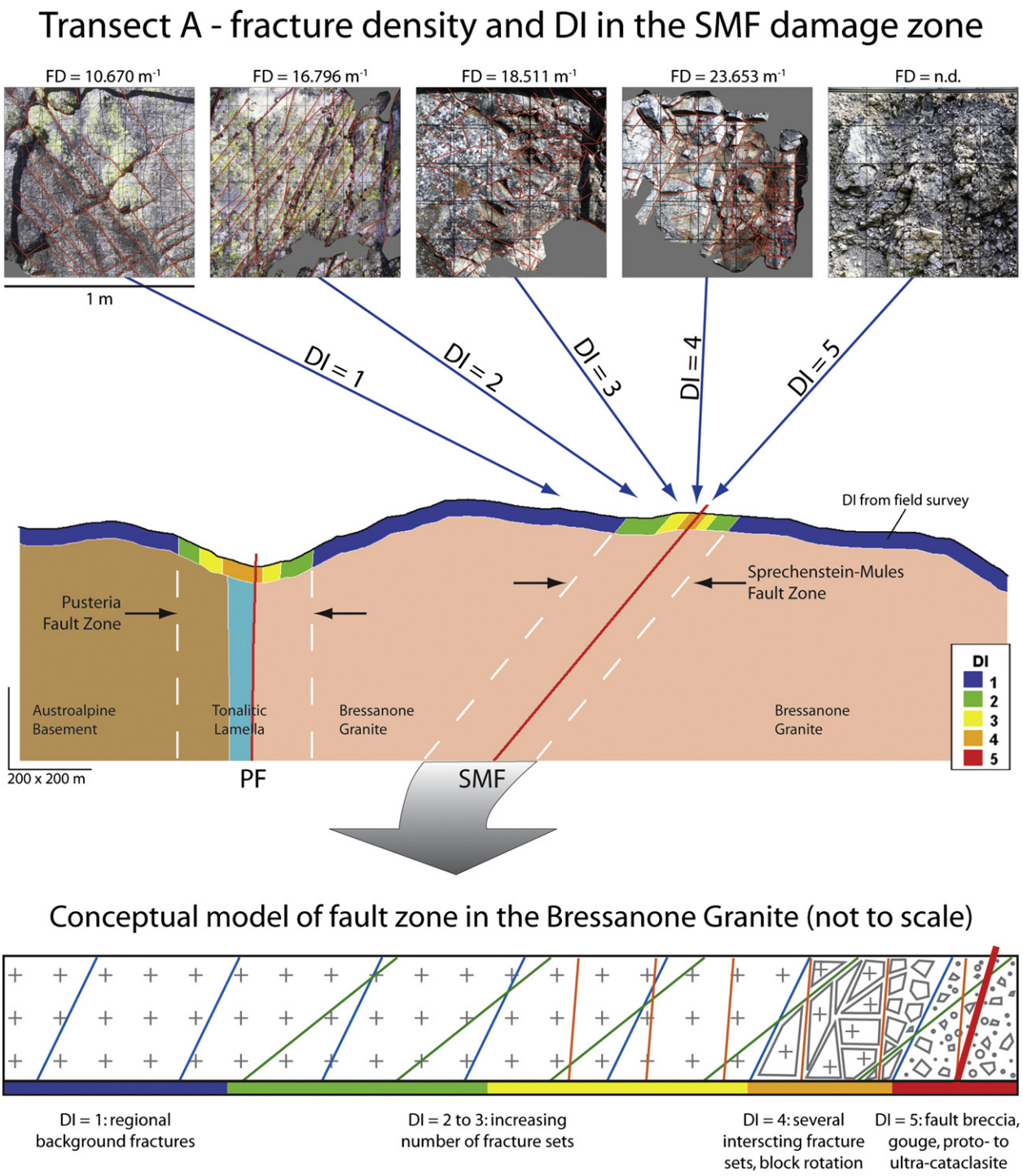

Fig. 2. Transect A across SMF (Passo Valles Skiing area), where it cuts across Bressanone Granite. The fault zone is evidenced by white dashed lines in lithological cross-section with DI data (color coded, shown along surface). Representative examples of fracture density surveys on 1 × 1 m square areas, and conceptual fault zone architecture model (not to scale) are shown above and below the cross-section. Thin lines, blocky pattern and thick red line in conceptual model schematically represent fracture sets, breccia/protocataclasite and fault core. (For interpretation of the references to color in this figure legend, the reader is referred to the web version of this article.)

The DI classification was tested and validated with fracture density data collected from selected outcrops and boreholes (e.g. Figs. 2–4). For both faults, going from the distal damage zone towards the core, both fracture density and DI increase steadily. In the very proximal damage zone and fault core (DI = 4 and 5 respectively), fracture density falls to "not defined" in field data and to zero in BHTV data, because the images cannot resolve the very pervasive fracturing of fault breccias, cataclasites and ultra-cataclasites (a similar behaviour is reported by Micarelli et al., 2006).

Lastly, the DI classification was applied to a 1:5.000 structural map covering the whole study area (ca. 40 km^2; Supplementary 1) and to boreholes (>2000 m continuous coring and BHTV data; Supplementary 2 and Supplementary 3). This very large dataset represents the input data for damage characterization in the 3D model.

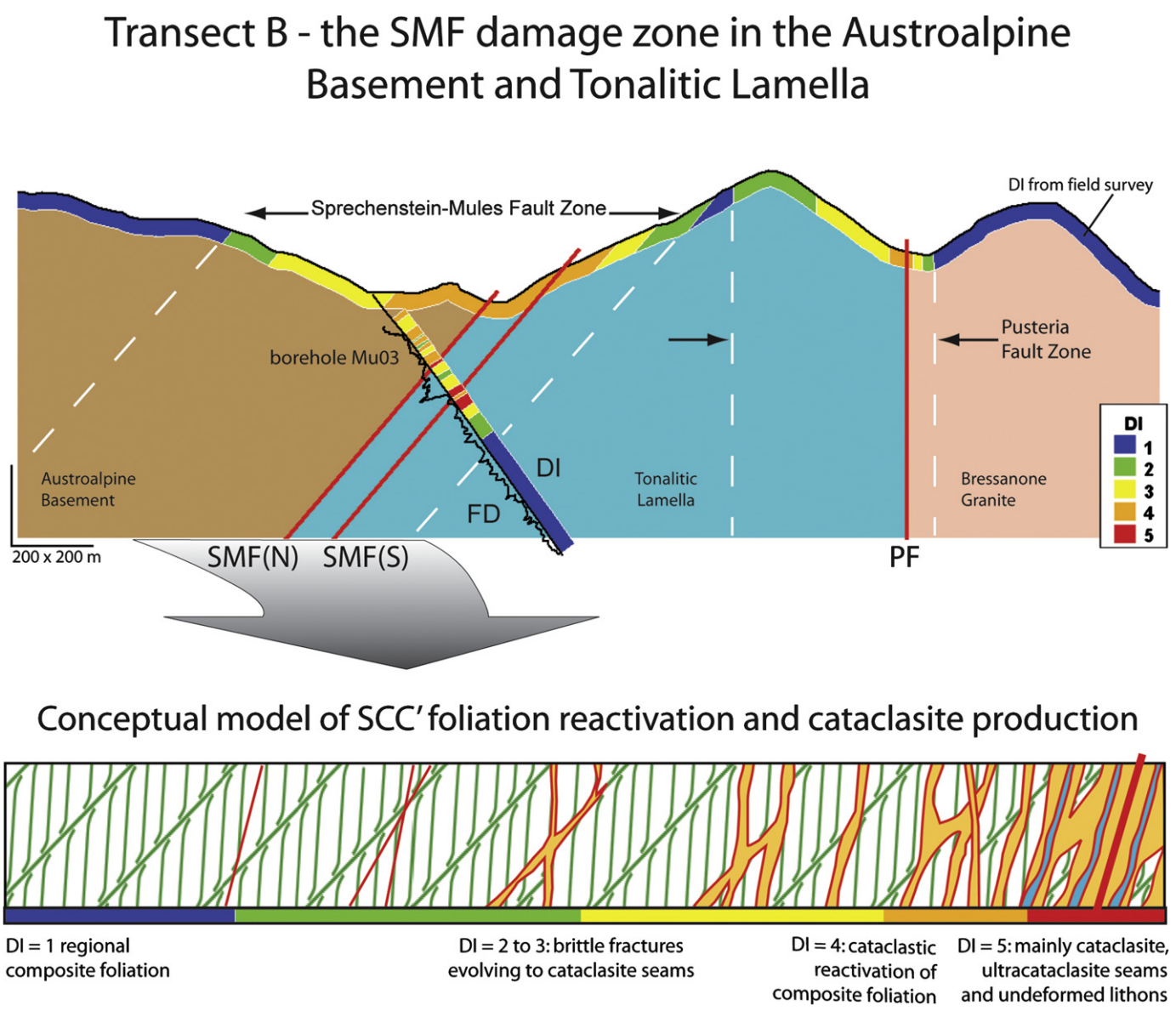

Fig. 3. Transect B across SMF (Leimgruben area and borehole Mu03), where it cuts across Austroalpine Basement and Tonalitic Lamella. The fault zone is evidenced by white dashed lines in lithological cross-section with DI data (color coded) collected at surface and along borehole. Fracture density log (FD) is added along borehole. Note that attitude of fault surfaces is very well constrained by surface and borehole data. Conceptual fault zone architecture model is not to scale. Thin green lines represent pre-existing mylonitic foliation. Thin lines, orange layers and thick red line schematically represent fracture sets, cataclasite seams and fault core. (For interpretation of the references to color in this figure legend, the reader is referred to the web version of this article.)

4.3. Fault slip data and paleostress

The paleostress field on the regional scale was derived from kinematic analysis (e.g., Petit, 1987) of meso-scale brittle faults in relatively un-deformed blocks to the N and S of the SMF and PF systems. Paleostress inversion was performed preferably with the Angelier's direct inversion method (Angelier, 1990) or by the NDA method (Spang, 1972) when field data did not allow a stable direct inversion solution.

4.4. 3D modelling techniques

A 3D geological model was reconstructed from the borehole and surface data by means of the geomodelling package gOcad®, in which the continuous fault surfaces of the fault network are discretized as triangulated surfaces and the volumetric properties of continuous blocks are represented by a regular 3D grid. This modelling framework matches common practice in the oil industry and theoretical conclusions by Ben-Zion and Sammis (2003), who state that mature fault zones are best described as continuous Euclidean surfaces in a solid continuum.

The gOcad® environment combines rigorous topology with robust interpolation techniques, making it possible to bypass the limitations of both purely geostatistical approaches and traditional CAD packages (see Appendix 1 and Mallet, 2002). The 3D fault network model was implemented by applying the procedures outlined in Appendix 2 (partly covered in Bistacchi et al., 2008). Surfaces reconstructed with this methodology are based on field data weighted according to their quality and on an explicitly imposed topology (e.g. crosscutting relationships between different fault strands) based on field observations.

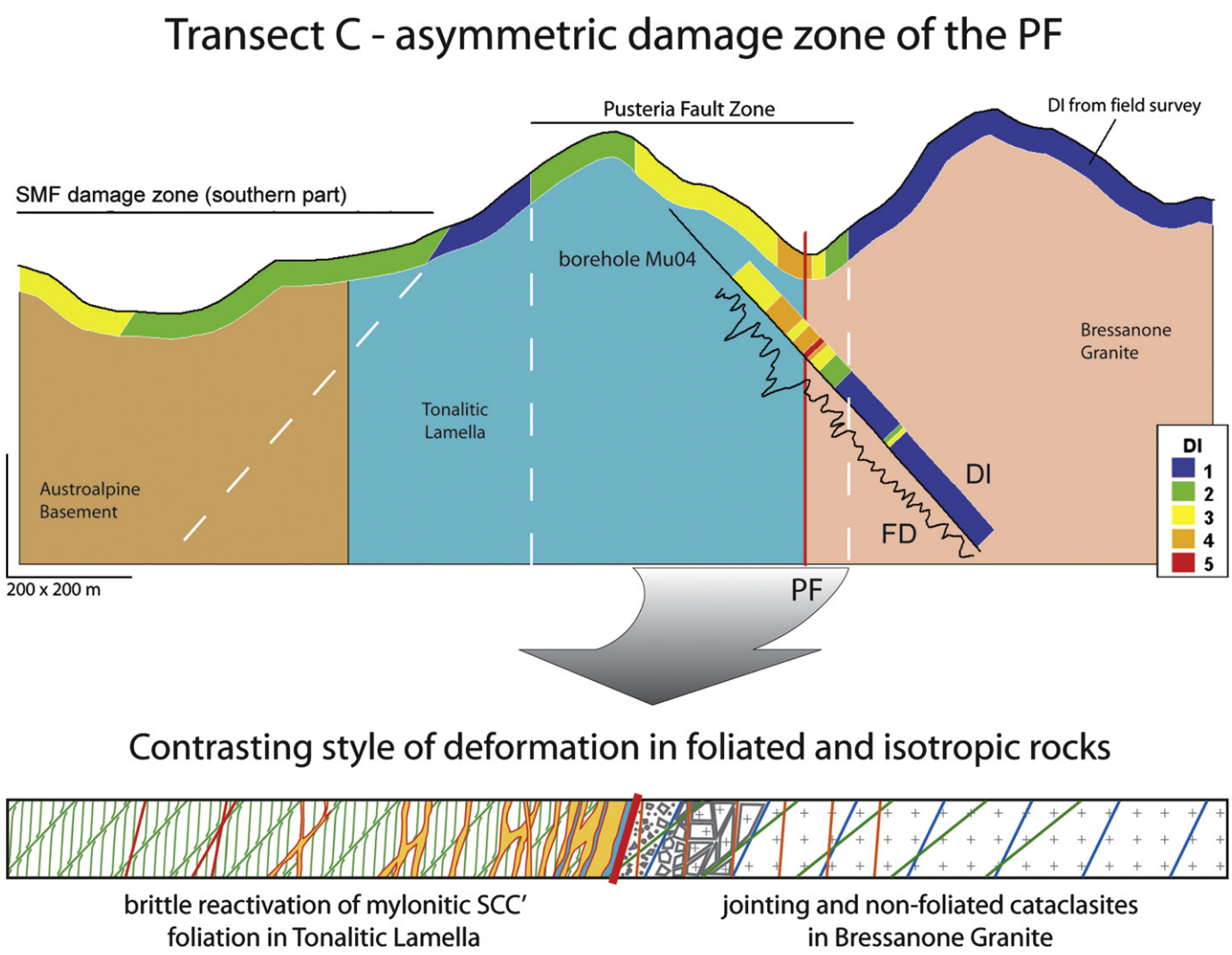

Fig. 4. Transect C across PF (Gelüge Graben area and borehole Mu04), where it cuts across Tonalitic Lamella and Bressanone Granite. The fault zone is evidenced by white dashed lines in lithological cross-section with DI data (color coded) collected at surface and along borehole. Fracture density log (FD) is added along borehole. Note that attitude of fault surfaces is very well constrained by surface and borehole data. Conceptual fault zone architecture model is not to scale. Thin green lines represent pre-existing mylonitic foliation. Thin lines, orange layers, blocky pattern and thick red line schematically represent fracture sets, ultracataclasite seams, breccia/protocataclasite and fault core. (For interpretation of the references to color in this figure legend, the reader is referred to the web version of this article.)

Having reconstructed the geometry and topology of the fault network, the next step was to populate the model with fault rocks and structural/geomechanical properties, defined either in surface or volumetric reference. Fault-rock classification and other properties (e.g. mean curvature) are represented as discrete functions defined on fault surfaces. These functions are discretized and stored at each node of the triangulated surfaces.

Damage zones are represented as fully-3D volumetric objects. The DI is modelled as a function defined on the damage zone volume and is discretized on a regular 3D hexahedral grid (voxet), which covers a $8 \times 4 \times 1.5$ km prism. The spatial resolution of this grid is $25 \times 25 \times 20$ m/voxet. The DI was interpolated with the DSI algorithm (Mallet, 2002), using field and borehole data as constraints. The interpolation was discontinuous across faults and geological boundaries (Fig. 8C), implying that DI values observed in the hanging wall of a fault do not influence this property in the footwall, and vice versa. In this way, asymmetrical damage zones and/or damage zones developing in different rocks on opposite sides of a fault can be modelled appropriately.

This data structure also allows fault-surface geological maps and juxtaposition maps (e.g. Graymer et al., 2005) to be reconstructed, in order to predict which tectonic unit is intersected by each fault in the 3D model space. This was done by means of procedures outlined in Appendix 3.

The level of uncertainty in 3D reconstruction is heterogeneous and may be estimated by means of the techniques illustrated in Bistacchi et al. (2008). A discussion can be found in Appendix 4, but in summary, although some uncertainty is implied in such a regional-scale model, spatial uncertainty is generally considered negligible at the model resolution ($25 \times 25 \times 20$ m/voxet) and does not affect the overall interpretation.

5. Results

5.1. Representative transects of PF and SMF

In this section, structural features observed during the mapping project are summarized by describing three representative transects, whose locations are shown in Fig. 1.

5.1.1. Transect A

At the Passo Valles Skiing area, the SMF cuts across the Bressanone Granite and shows quite continuous exposure of both core and damage zones. This transect was selected to show how fracturing in the damage zone develops as the fault core is approached (Figs. 1 and 2). The homogeneity and isotropy of the Bressanone Granite ensures that lithological variability does not affect the development and evaluation of fault-related fracturing. Although fracture density increases almost steadily (but not linearly) towards the fault core, it is noteworthy that, as regards the distal damage zones, this parameter increases mainly due to increased numbers of fracture sets rather than to decreased fracture set spacing (Fig. 2, and Supplementary Material for supporting data). In fact, when the number of fracture sets, with approximately constant spacing, increases, the cumulative fracture density also increases. The distal damage zone is characterized by rock masses with DI = 2–3 and is about 200 m thick. In this volume, fractures can be classified according to their attitude and kinematics, and T and R′ prevail on other kinds of fractures. Both tensional and Riedel fractures quite often show thin (<1 mm) coatings of quartz + epidote ± chlorite. The proximal damage zone is an almost chaotically fractured rock mass with DI = 4–5 (Fig. 2). Classifying fractures based on attitude and kinematics is increasingly difficult, and quartz + epidote ± chlorite coatings are common. Only in sectors very close to the fault core (ca 10–15 m from the principal slip surface) does spacing begin to decrease visibly, fracture sets become almost indistinguishable because of a multitude of mutually intersecting striated surfaces, and clasts are strongly rotated. The fault core is locally exposed and is characterized by a non-foliated fault gouge horizon ca. 5 m thick, classified as DI = 5.

5.1.2. Transect B

This transect represents a synthesis of surface data from the Leimgruben area and observations from the Mu03 borehole (Figs. 1 and 3). In this sector the SMF brings the Austroalpine phyllonitic paragneiss into contact with the Mules foliated tonalites. The SMF is complicated here by a km-scale array of stepovers, bounded by principal fault surfaces with attitudes around dip/dip-direction 60/020. Relay zones are characterized by minor high-angle reverse faults, which represent the linkage between various principal faults (Fig. 1).

At distances of <600 m from the main SMF surface, the pre-existing mylonitic composite fabric of the Austroalpine para- and orthogneiss (N- to NNE-dipping SCC' surfaces) is progressively overprinted by fracturing, characterized by 4–5 fracture sets with a ca. 50 cm spacing (see Supplementary Material). Noteworthy, veining is virtually absent. This volume is classified as DI = 2–3. Approaching the main fault surface, about 100–150 m north of the contact with the Tonalitic Lamella, localized mm-thick cataclasite to ultracataclasite seams overprint the phyllonitic composite SCC' foliation. This proximal damage zone is classified as DI = 4. Spacing of cataclasite layers generally decreases from 1–2 m to < 1 cm towards the core of the SMF, although the distribution of cataclastic deformation appears to be irregular in the field and in the borehole, leaving meter-thick phyllonite lenses (lithons) relatively less deformed with respect to adjacent bands (≤1 m thickness) of strongly cataclastic phyllonites. For example, in borehole Mu03, localized high-strain zones (DI = 4) are observed between 65 and 90 m from the fault core, interlayered with lithons of less deformed phyllonitic paragneiss (DI = 3; see Supplementary Material). These high-strain zones are characterized by up to 2-m-thick bands of foliated cataclasites, concordant with the phyllonitic foliation.

In its central part, the transect crosses the relay volume between two major segments of the SMF. The northern segment, which marks the Austroalpine–Tonalitic Lamella boundary, is associated with a 2–5 m thick fault core composed of foliated ultracataclasites with localized incohesive black striated surfaces, which can be observed in both outcrops and the Mu03 borehole (DI = 5). The relay volume itself is composed of foliated tonalites (DI = 3) obliquely overthrust by the Austroalpine phyllonites along secondary high-angle reverse faults confined between the major segments. The southernmost fault core is continuously exposed in the Mu03 borehole, where it is marked by up to 5-m-thick foliated cataclasites, overprinting phyllonitic tonalites (DI = 5). Localized millimetric ultracataclasites developing along black, striated, shiny slickensides are frequently interleaved with the foliated cataclasites.

In the Tonalitic Lamella, the damage zone is characterized by intense fracturing (more than 4 fracture sets), which progressively decreases in intensity with increasing distance from the fault cores. Fractures are generally decorated by zeolites, quartz and calcite fillings, ranging in thickness from a few hundred μm to up to 3 cm. Depending on fracture orientation, these fillings may develop as slickenfibres along shear fractures (with kinematics coherent to that of the main faults) or as blocky crystals in purely tensional veins. In the distal damage zone, fractures and veins simply overprint the pre-existing high-temperature foliation. Approaching the main slip surfaces, zeolite/quartz/calcite veins and fractures also overprint earlier tonalite-derived proto- to ultracataclasites, thus they may be related to a late- to post-kinematic stage of fluid circulation, possibly favoured by increased permeability in the damage zones.

The Tonalitic Lamella damage zones extend for at least 100 m from each principal segment of the SMF. This means that, in the SMF relay zones, where at least two principal slip surfaces occur, the fault zone (core + damage) is very large, as corroborated by the 220 m fault zone thickness encountered in borehole Mu03 within foliated tonalites.

5.1.3. Transect C

This transect represents a synthesis of surface data from the Gelüge Graben area and observations from the Mu04 borehole (Figs. 1 and 4), where the PF brings the Tonalitic Lamella into contact with the Bressanone Granite. The PF shows the same structural aspects and fault-rock thickness at Gelüge Graben and in the Mu04 borehole, located 2 km to the east, and it is reasonable to predict that the PF maintains its distinctive features throughout the study area.

The damage zone in the Tonalitic Lamella is 350 m thick and is characterized by a pervasive network of fractures similar to that described for the SMF in transect B. Approaching the Bressanone Granite contact, within 30–50 m of the principal slip surface in the Mu04 cores, fracturing becomes more pervasive and several thin green cataclastic layers (<1 cm thick) can be observed (DI = 4). The fault core (DI = 5) is characterized by fault rocks deriving from both the Tonalitic Lamella and Bressanone Granite. The former, just like those developing along the SMF, are foliated cataclasites up to 5 m-thick, with localized foliated ultracataclasite and gouge layers up to 0.5 m thick. The latter are massive green cataclasites (due to the presence of epidote and chlorite), interleaved with less deformed protocataclasite metric lithons, forming a continuous layer 10–15 m thick.

Along the transect, on the surface and in the Mu04 borehole, the Bressanone Granite displays a poorly developed damage zone (Fig. 4). At distances exceeding 70 m from the fault core, the granite never displays more than three intersecting fracture sets and often appears massive (DI = 1). Veining is virtually absent within this zone. Only in the most proximal damage zone (ca. 10–15 m from the fault core) the fault rock is a protocataclasite, where cm-sized rotated fragments of granite are separated by thin (less than 1 cm thick) wavy cataclastic horizons (DI = 4).

5.2. Fault-rock mineralogy and microstructure

Field work was integrated with fault-rock microstructure and mineralogy by means of optical and SEM back-scattered electron

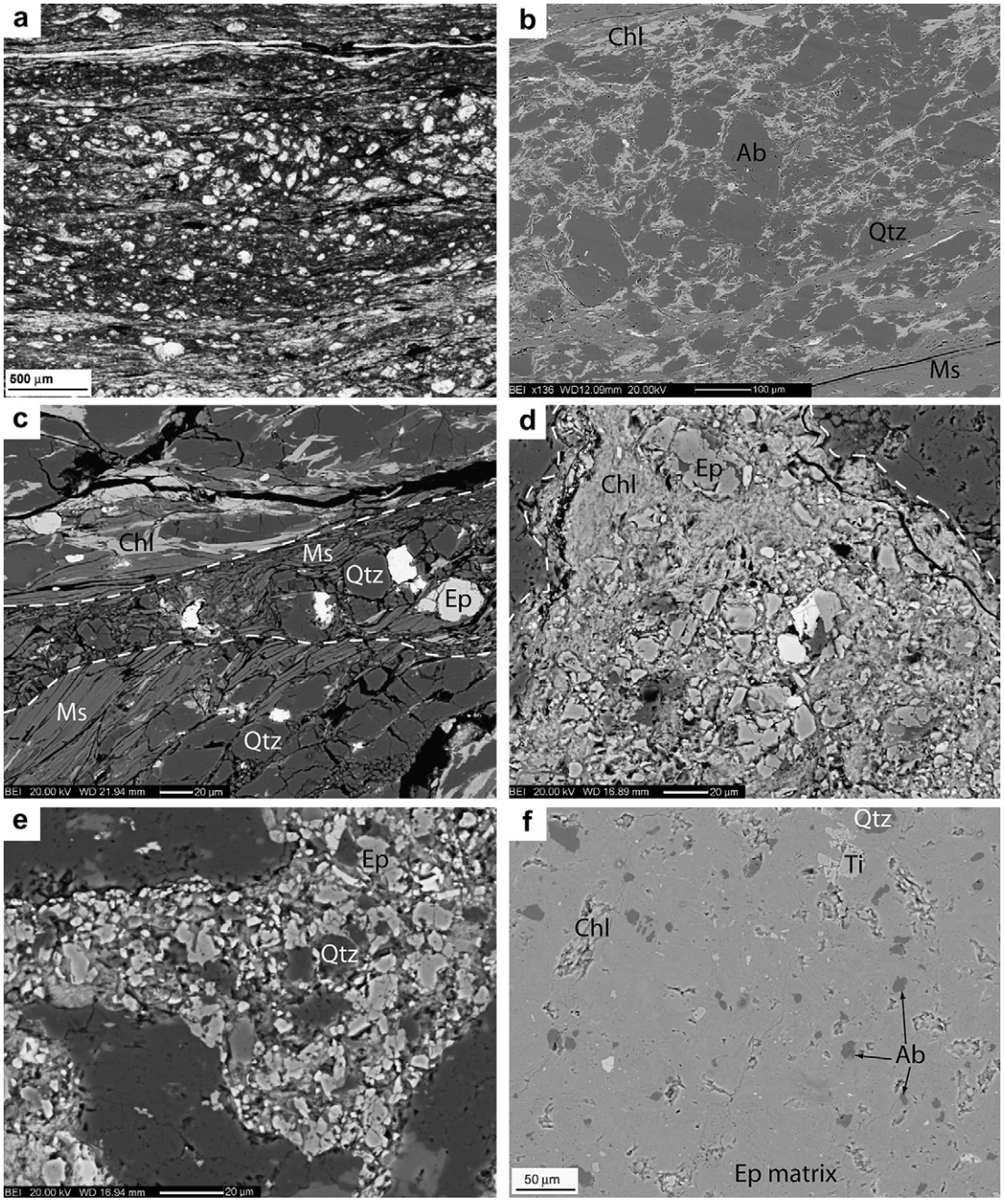

Fig. 5. Representative microstructures of fault rocks. Mineral abbreviations: Chl = chlorite, Ab = albite, Qtz = quartz, Ms = muscovite, Ep = epidote, Pl = plagioclase, Kfs = K-feldspar, Ti = titanite. (a) Cataclasite layer along foliation of Austroalpine phyllonite. Clasts are of albite and quartz. Mica-rich layers are composed of predominant chlorite and muscovite, with local seams of opaques. Optical microscope, crossed polars. (b) SEM back-scattered electron image of the cataclasite shown in (a). (c) SEM back-scattered electron image of a cataclasite along a C surface in tonalite-derived phyllonite encountered in Mu03 borehole. (d) SEM back-scattered electron image of an incohesive black slip surface in phyllonitic tonalite. Note relative abundance of chlorite with respect to other phases. (e) SEM back-scattered electron image of a localized wavy cataclasite layer within proto-cataclasite 10 m from the PF fault core. (f) SEM back-scattered electron image of massive green cataclasite derived from Bressanone Granite in PF fault core. The fine-grained matrix mostly consists of epidote with minor chlorite.

microscopy, and X-ray powder diffraction analysis of material from black ultracataclastic seams. The main results for each geological unit are reported in the following subsections.

5.2.1. Austroalpine paragneiss

The Austroalpine paragneiss display a pervasive N- to NNE-dipping phyllonitic foliation subparallel to the PF (Fig. 1). This foliation is composite (SCC') and consists of a mm-scale compositional layering with alternating granoblastic quartzo-feldspathic layers and phyllosilicate-rich domains. Cataclasites up to 0.5 cm thick occur concordant with the phyllonitic foliation and preferentially develop along the quartz-feldspar layers. They consist of angular and rounded clasts of quartz and albite dispersed in a foliated matrix of predominantly chlorite and muscovite (Fig. 5a and b). The pre-existing mica-rich layers of the phyllonites do not display clear brittle reactivation, but typically contain up to 50 μm thick seams of opaques (Fig. 5a). Similar cataclasite seams reactivate C and C′ surfaces. The combined reactivation of the composite phyllonitic foliation results in an anastomosing network of cataclastic seams which are very pervasive in the fault core, but

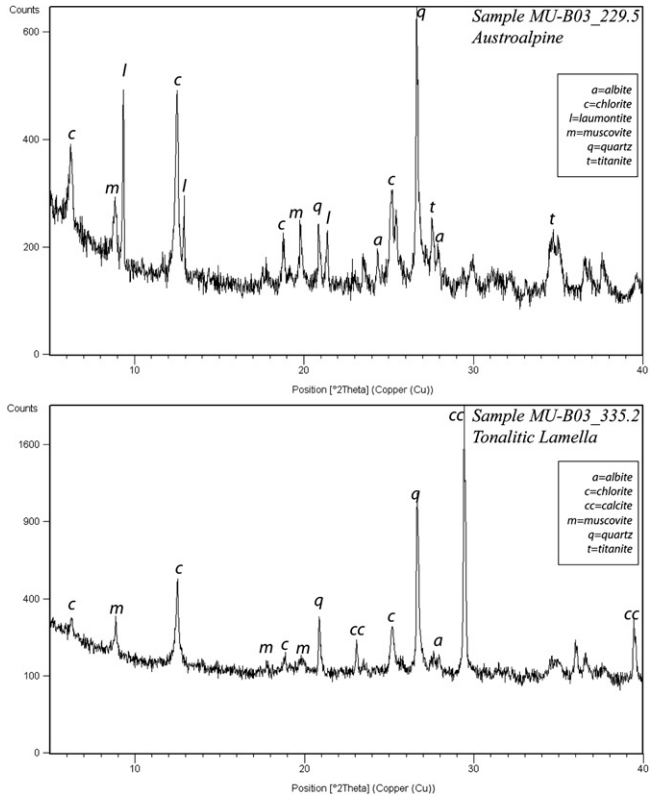

Fig. 6. XRPD analysis of incohesive black slip surfaces within Austroalpine and Tonalite phyllonites.

which also occur, as very localized and confined horizons, in the proximal damage zone.

Ultracataclasite horizons, in both core zone and damage zones, frequently appear as localized, incohesive, black striated or mirror-polished shiny slickensides (Fig. 5). XRPD analyses of the very fine-grained material found along these surfaces revealed the presence of chlorite, muscovite, quartz, albite, K-feldspar, and titanite. The analysis identified laumontite as the zeolite in veins (Fig. 6).

5.2.2. Tonalitic Lamella

Cataclastic layers within the non-mylonitic Tonalitic Lamella are typically concordant with the high-temperature foliation. They are 100 μm–2 mm thick and consist of angular fragments of quartz > saussuritized plagioclase > hornblende > K-feldspar, dispersed in a fine-grained matrix (<10 μm) of quartz, epidote, chlorite, muscovite and titanite. Minor cataclastic bands crosscut the high-temperature foliation at a low angle.

The tonalite-derived greenschist-facies phyllonites observed in the Mu03 borehole display a composite SCC' foliation, with alternating 100–200 μm thick muscovite- and chlorite-rich bands (with minor epidote and titanite) and elongated ribbons of recrystallized quartz. Cataclasite layers developing in these rocks overprint the S, C and C′ surfaces and consist of fragmented clasts of quartz, epidote, titanite and chlorite in a fine-grained (<10 μm) chlorite-rich matrix (Fig. 5c).

In the Mu03 borehole, some mm-thick, poorly cohesive, black striated slickensides, similar to those observed within the Austroalpine basement rocks, were observed in the proximal damage zone. They form a pervasive network on the decimeter scale, with most of the surfaces parallel to the pre-existing foliation. Material from these surfaces consists of less than 20 μm sized clasts of quartz, albite, epidote and titanite within an ultrafine-grained (<5–10 μm) matrix predominantly of chlorite (Fig. 5d). XRPD analysis confirmed that the black surfaces are composed of chlorite, muscovite, quartz, albite, K-feldspar and titanite, like the shiny black surfaces in the Austroalpine phyllonites (Fig. 6). Calcite was most likely a vein-filling phase.

5.2.3. Bressanone Granite

Granite protocataclasites occurring in the proximal damage zone of the PF consist of angular lithic clasts of quartz, feldspars, epidote and chlorite up to 0.5 cm in size, and in a fine-grained matrix (<10 μm grain size) of epidote, chlorite and minor titanite (Fig. 5e). The massive green cataclasites at the fault core are characterized by extensive precipitation of epidote, which forms most of the cataclasite matrix (Fig. 5f). Lithic fragments are made of quartz, albite, epidote and minor titanite. Chlorite is present both as a minor component of the cataclasite matrix as well as in up to 100 μm long clasts. The extensive precipitation of epidote may be related to the widespread presence of quartz + epidote ± chlorite coatings on fractures in the damage zones.

5.3. Paleostress

Fig. 7 shows stress-inversion data from a region surrounding the study area. These results are considered to be a good approximation of a far-field stress state during the main brittle activity of the SMF. The least compressive stress tensor eigenvector σ_3 is very stable, almost always E-W sub-horizontal. The intermediate and most compressive stress tensor eigenvectors σ_2 and σ_1 show frequent permutations, being either sub-vertical or N-S sub-horizontal, consistent with repeated switching between normal and strike-slip faulting regimes. This is consistent with the σ_1 and σ_2 being of similar magnitude and a high stress ratio $\Phi = (\sigma_2-\sigma_3)/(\sigma_1-\sigma_3) \approx 0.6–0.7$ (Angelier, 1990). It must be noted that the inferred regional stress field is consistent with the Miocene kinematic pattern, dominated by E-W extension during continuing N-S convergence (e.g. Selverstone, 1988, 2005; Ratschbacher et al., 1991; Fügenschuh et al., 1997; Frisch et al., 2000).

5.4. 3D model of fault zone

This section describes the 3D model of fault zone architecture in terms of the topology of the fault network, fracturing in damage zones (DI value) and the occurrence, in fault cores, of different fault rocks developing from different protoliths.

5.4.1. Topology of fault network and relationships with paleostress analysis

The 3D fault network model clearly shows the complex intersection relationships between the older PF and the younger SMF (Fig. 8). The trace of the PF is offset with a dextral separation of ca. 1 km along the SMF, but the vertical component of the SMF cumulative slip vector cannot be reconstructed here because the PF is sub-vertical. Instead, when we consider the offset in the reconstructed hinge line of the Mules Syncline, we can draw a cumulative slip vector with plunge/trend = 21/311, showing a total dextral/reverse offset of ca. 1.5 km. The horizontal component of this vector equals the horizontal separation calculated for the PF, validating this kinematic model. The cumulative slip vector is almost perpendicular to the axis of the Leimgruben stepover. Hence this may be defined as a contractional jog (Scholz, 2002), which represents a strong impediment to accumulation of deformation along the SMF.

The best-fit planar surface approximating the SMF has dip/dip-direction = 50/022. It is possible to calculate the tangential (shear) and normal traction components, resolved on this surface, of the

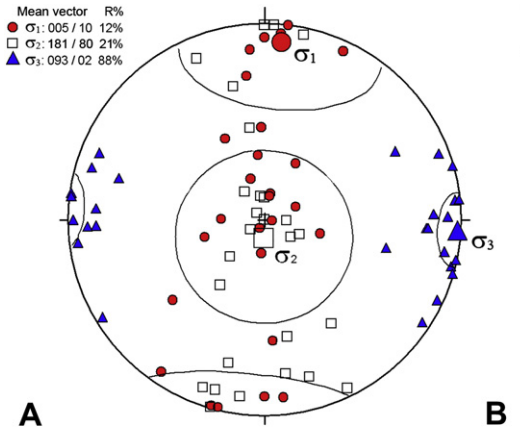

outcrop ID	σ1 trend	σ1 plunge	σ2 trend	σ2 plunge	σ3 trend	σ3 plunge	stress ratio	inv. method	No. data	misfit < 15°	quality	easting	northing
0701	236	83	25	6	115	4	0.61	NDA (35)	7	43%	3	686060	5196582
0702	164	18	341	72	74	1	0.65	NDA (45)	6	83%	2	687100	5195386
0704	200	10	67	76	292	10	0.40	DIR-INV	6	83%	2	687881	5194951
0706	196	1	104	66	286	24	0.78	NDA (70)	8	100%	4	689136	5196611
0707	124	77	360	8	268	11	0.46	NDA (45)	11	30%	4	689893	5195410
0708	113	89	7	0	277	1	0.80	NDA (32)	7	71%	2	690167	5206892
0709	214	57	353	27	93	19	0.65	DIR-INV	6	50%	2	690616	5198301
0710	188	10	12	80	278	1	0.62	NDA (25)	6	67%	3	690948	5203624
0712	147	37	334	52	239	4	0.56	NDA (60)	6	83%	2	691457	5194106
0715	0	81	214	7	123	5	0.49	NDA (34)	6	83%	3	691695	5196963
0718	337	12	186	76	69	6	0.71	DIR-INV	6	100%	2	692539	5191814
0719	194	26	354	63	100	8	0.81	NDA (70)	7	57%	3	693105	5191515
0724	325	76	180	11	89	8	0.84	DIR-INV	17	76%	4	693648	5191867
0728	312	86	194	2	104	3	0.88	DIR-INV	16	63%	4	693927	5192451
0730	223	69	355	14	88	15	0.36	DIR-INV	12	75%	4	694098	5192669
0733	196	11	12	79	106	1	0.44	NDA (40)	6	67%	3	694249	5201798
0736	172	22	29	63	268	15	0.26	DIR-INV	10	70%	4	694510	5191989
0740	350	80	174	10	84	1	0.58	NDA (16)	20	70%	4	695881	5200528
0743	347	31	229	38	103	37	0.36	NDA (15)	6	83%	2	696702	5190782
0748	154	5	254	64	62	26	0.35	NDA (50)	10	60%	3	697408	5191335
0751	92	81	196	2	287	9	0.84	DIR-INV	8	75%	4	698535	5193364
0753	113	74	5	5	274	15	0.28	NDA (36)	5	60%	2	698943	5194080
0755	3	1	271	72	93	18	0.34	DIR-INV	6	66%	2	699680	5197578
0757	12	4	210	86	102	1	0.58	DIR-INV	16	81%	4	699862	5189906
0758	169	39	358	51	263	5	0.58	DIR-INV	7	30%	2	699978	5194785
0759	360	1	98	87	270	3	0.54	NDA (75)	9	78%	4	700105	5184314
0761	351	51	176	38	84	3	0.70	DIR-INV	7	86%	3	700408	5189104

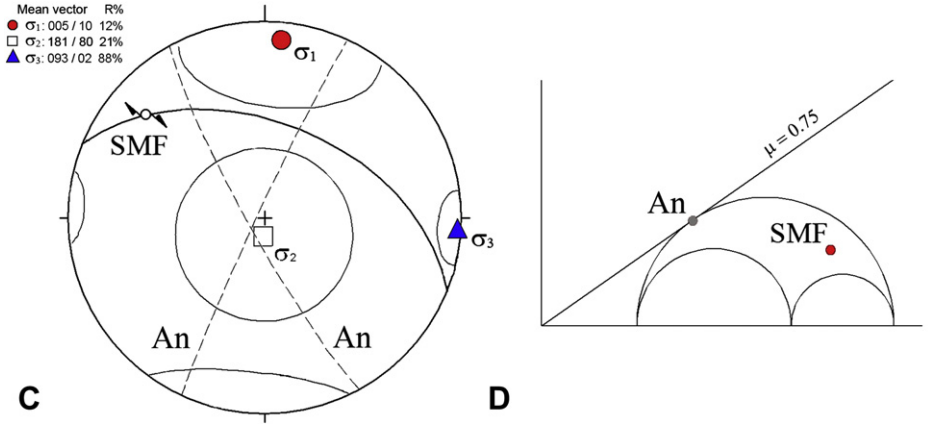

Fig. 7. Paleostress data synoptic stereoplot and data table. (A) σ_1, σ_2 and σ_3 axes at selected outcrops and inferred regional-scale mean values (large symbols). σ_3 is very stable. Several cases of σ_1–σ_2 permutations are evidenced by σ_1 axes occurring in a near-vertical attitude. (B) Data table. Column "inv. method" indicates stress-inversion method which gave best results in each site (NDA = Natural Dynamic Analysis – Φ angle in brackets – Spang, 1972; DIR-INV = Direct Inversion – Angelier, 1990). Column "misfit < 15°" indicates fraction of fault slip data showing a misfit angle < 15° (Angelier, 1990). Column "quality" indicates overall quality evaluation on a scale from 1 to 4. (C) Paleostress data synoptic plot. σ_1, σ_2 and σ_3 regional-scale mean values, SMF mean plane and slip vector, and hypothetical Andersonian fault planes are represented. (D) A dimensional Mohr-space representation with poles representing SMF and hypothetical Andersonian faults (an).

regional-scale reduced stress tensor (Fig. 7). The tangential component is oriented 25/315, thus forming an angle of only 5° with the cumulative slip vector. Given the approximations implied in this kind of analysis, the observed misfit is considered to be very small and we may conclude that the cumulative slip vector matches very well the paleostress estimates for the time of deformation. However, the tangential stress component is quite small with respect to the normal component ($\tau/\sigma_n = 0.27$), as is evidenced in the Mohr space (Fig. 7), and implies that the SMF fault behaves like a weak fault relative to the surrounding (strong) crust (e.g. Rutter et al., 2001). Angles formed by the mean fault plane with the σ_1, σ_2 and σ_3 axes and with the plane containing the σ_1 and σ_3 axes are 31°, 56°, 19° and 38° respectively. The orientation of optimal Andersonian planes (Anderson, 1951) for this state of stress would be (dip/dip-direction) 87/295 and 83/241, and the above mentioned angles $45°-\Phi/2 = 27.5°$, 0°, $45°+\Phi/2 = 62.5°$ and 90°, respectively (Φ here is the friction angle ≈ 35°). Hence, the fault is far from an Andersonian orientation with respect to the stress field.

There are considerable differences in the topology of the PF and SMF. The parameters considered in this analysis are curvature of single fault surfaces and the overall arrangement of fault segments, e.g. whether they constitute bends, jogs or stepovers, etc. The mean principal normal curvature of a surface, being the mean value of the maximum and minimum eigenvalues of the normal curvature tensor (principal normal curvatures), is useful in characterizing the shape of fault surfaces in a synoptic view (Pollard and Fletcher, 2005). This property can easily be calculated for any discrete surface by differential geometry (Mallet, 2002).

The PF is quite planar in the study area, and is always characterized by a limited mean curvature and does not show bends or stepovers. Instead the SMF is composed of slightly "wavy" segments, with limited mean curvature, separated by relatively complex stepovers (Fig. 8). It should be noted that the availability of borehole data in the middle of the Leimgruben contractional jog allowed this structure to be reconstructed to a high degree of accuracy.

The Leimgruben stepover relay volume crossed by the boreholes is characterized by several cross-faults and defines a contractional duplex, which is not completely breached. The overlap is ca. 1500 m and separation ca. 200 m (Fig. 8). Mean curvature is higher in the stepover volume (Fig. 9), where faults tend to increase their curvature and bend outwards, as commonly observed in other fault zones and in numerical models (e.g. Segall and Pollard, 1980; Sibson, 1986).

5.4.2. Fracturing in damage zones

Damage zones are generally characterized by a steady decrease in the DI value from the core to the periphery. However, their thickness varies markedly along strike and shows important asymmetries and heterogeneities, spatially related to: (1) the

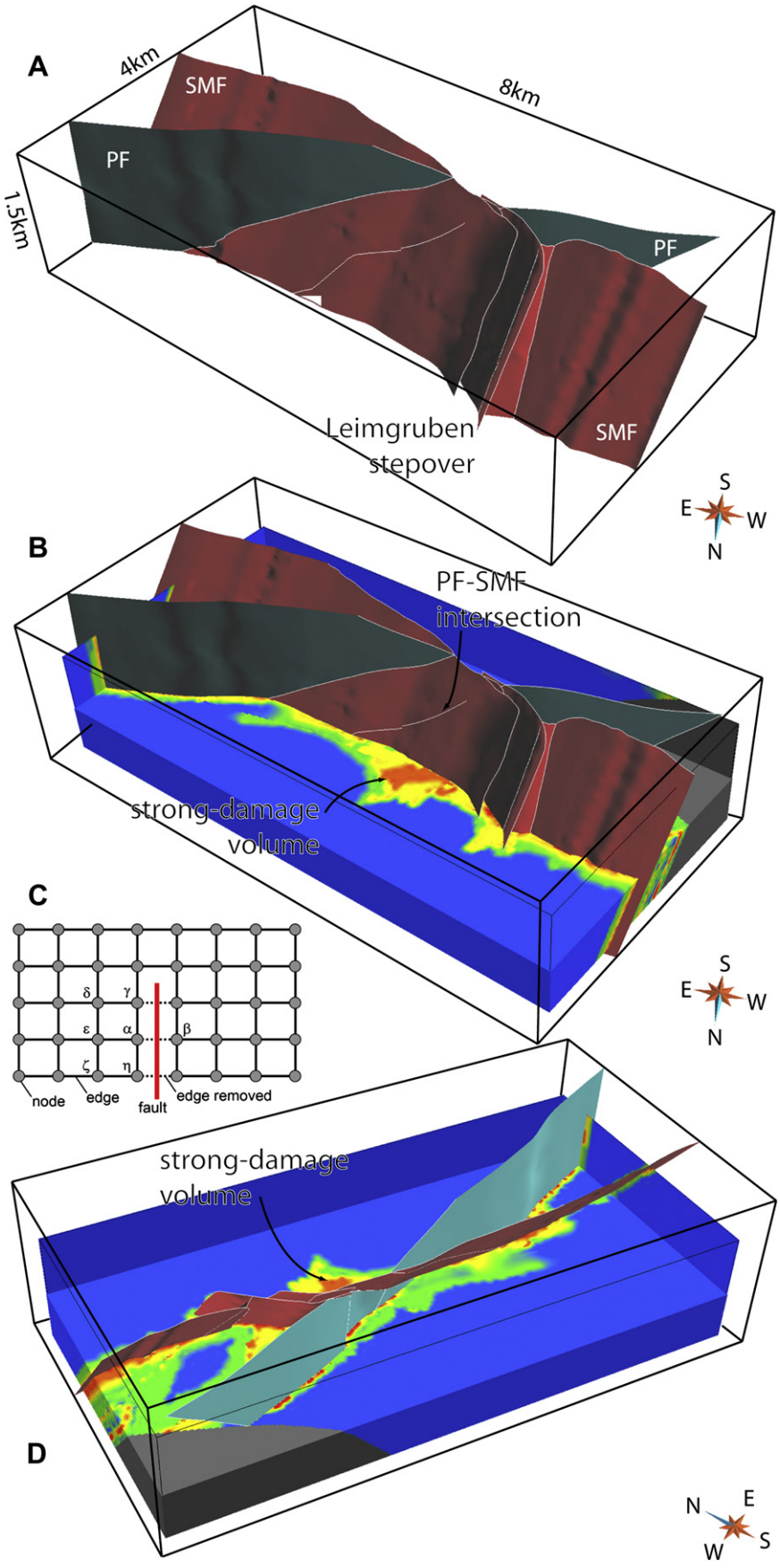

Fig. 8. (A) 3D model of fault network. View from NW. SMF and PF in red and light blue, respectively. Model covers a volume of ca. 10 × 5 × 1.5 km (B, D) Fault network and interpolation of DI on a 3D regular hexahedral grid. View from NW (B) and SW (D). 3D grid is 8 × 4 × 1.5 km. (C) Interpolation on a 3D regular grid (voxet) with grid connectivity broken across faults (topology of model reflects fault zone architecture). If node β lies on other side of a fault with respect to node α, node β does not belong to neighbourhood N(α) of α and is not used in interpolation at α. Nodes γ, δ, ϵ, ζ, and η belong to N(α) and influence interpolation. In this way, asymmetrical damage zones, and/or damage zones developing in different rocks on opposite sides of a fault can be modelled appropriately. (For interpretation of the references to color in this figure legend, the reader is referred to the web version of this article.)

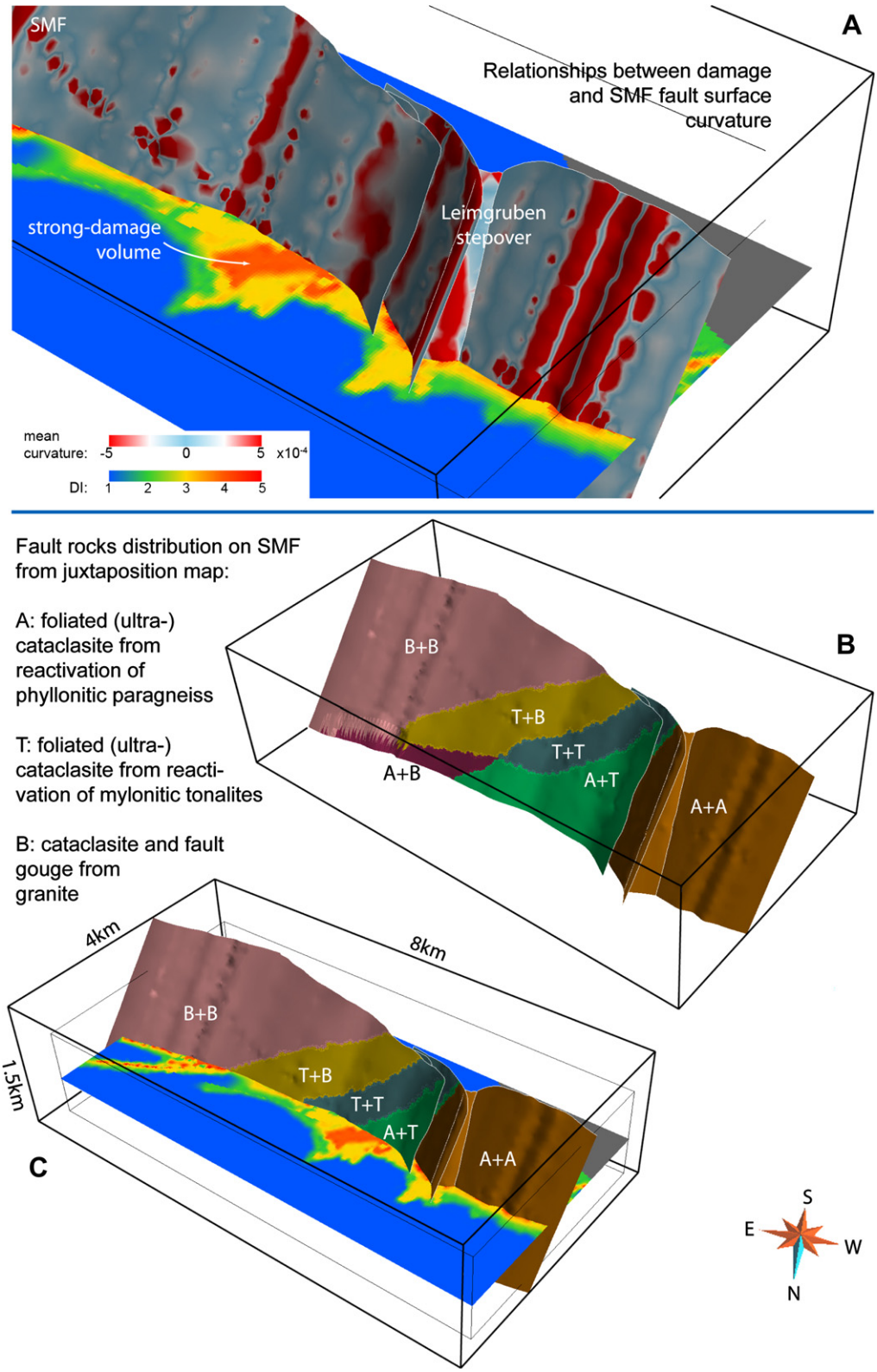

Fig. 9. (A) Mean curvature of SMF and horizontal slice across DI interpolation 3D grid in Leimgruben stepover region (same view angle as in Fig. 8a). Note high-damage lobe propagating asymmetrically in extensional quadrant. (B) Map of fault rocks in core zones derived from juxtaposition map. A, T and B indicate fault rocks derived from Austroalpine Basement, Tonalitic Lamella and Bressanone Granite respectively. The fault-rock map results from different combinations of these rocks. (C) Comparison with DI shows no relationship between damage and possible rheological boundaries in the fault core. Wireframe indicates extension of 3D volumetric model.

occurrence of different lithologies on opposite sides of fault segments and (2) the geometrical complexity of the arrangement of fault segments.

Considering only the best represented lithologies, damage zones are narrowest in the Bressanone Granite, thicker in the Tonalitic Lamella, and thickest in the Austroalpine Basement (Fig. 8). Deformation tends to be strongly localized in the homogeneous Bressanone Granite, producing thin damage zones and a steep gradient in the DI value, going from the highest at the core to the lowest at the boundary of the fault zone, where only regional-background fracture sets can be found. This behaviour is constantly repeated along both PF and SMF, and this is not surprising because the deformation conditions did not vary greatly in the Bressanone Granite during the time-span considered.

The Tonalitic Lamella never appears outside the damage zones of either PF or SMF and, near the intersection, damage due to the two fault zones is superimposed, resulting in an unusually large volume of highly damaged material (Fig. 8b, d). Since the outer boundary of the damage zones is never reached, a lower bound to their thickness can be defined only from the half-thickness of the Lamella wedge between the SMF and the western segment of the PF, as shown in Fig. 8. This is much greater (almost twice/three times as wide) than the thickness of the facing damage zone in the Bressanone Granite. Accordingly, the DI gradient is lower than in the Bressanone Granite.

Substantial heterogeneities in DI values were observed along the SMF. A very marked and extensive lobe-shaped damage volume developed in the Austroalpine basement rocks at the hanging wall of the SMF, in close proximity to the Leimgruben contractional jog (strong damage volume in Figs. 8 and 9). This lobe originates about 700 m east of the tip line of the northernmost fault surface defining the relay volume, and extends eastward from there, in the extensional quadrant (i.e. the quadrant containing σ_3) of the dextral SMF. In general, steeper DI gradients (faster damage decay) are observed along planar SMF fault segments, as well as in the footwall block of the SMF.

The 3D model allows the degree of damage to be evaluated even where a single fault-surface crosses lithological contacts between different units. In particular, the north face of the SMF "exposes" the primary contact between the Tonalitic Lamella and the Austroalpine basement, whereas the south face "exposes" the Tonalitic Lamella/Bressanone Granite tectonic boundary along the PF. The 3D model shows that the degree and distribution of damage does not reveal any clear correlation with these lithological boundaries.

5.4.3. Fault cores

As the first-order control on fault rocks in core zones is exerted by protolith composition, we can predict to some extent which fault-rock associations will occur in 3D by using the juxtaposition map. The results of this analysis for the SMF and PF are shown in Fig. 9 as "fault-rock maps". Due to the complex relationships between SMF, PF and the northern boundary of the Tonalitic Lamella, the SMF fault-rock map shows elongated oblique patches with rather different fault rocks, which extend obliquely to the dip, and also to the slip vector. Each patch of the fault surface is characterized by the juxtaposition of different tectonic units and hence by the development of different fault rocks.

The PF fault-rock map shows similar juxtaposition relationships to those of the SMF map, but the geometry of fault-surface patches is simpler, because their geometry is defined only by the cross-cutting relationships between the northern boundary of the Tonalitic Lamella and the PF itself. As already shown in the previous section for lithologic boundaries, no clear relationship is seen in the 3D model between fault rocks mapped for the SMF or PF and the distribution of fracturing in damage zones, as represented by DI.

5.4.4. Scaling parameters

The displacement/length (D/L) ratio for the PF cannot be defined (displacement unknown – length in excess of tens of km), but the same ratio for the SMF is approximately 0.075 (D/L = 1.5 km/20 km). Considering the displacement/thickness (D/T) and thickness/length (T/L) ratio, the 3D model yields quite variable results. The thickness of the damage zone in the Leimgruben contractional jog of the SMF is nearly 1000 m, whereas the same parameter along smooth rectilinear segments of the SMF and PF is ca. 200 m. The D/T for the SMF varies between 1.5 (jog) and 7.5 (rectilinear segments) and the T/L ranges between 0.05 (stepover) and 0.01 (rectilinear segments). The D/T of the PF is at least one order of magnitude larger than that of the SMF, being > 50 ($D > 10$ km, $T = 200$ m).

6. Discussion

The Pusteria (PF) and Sprechenstein-Mules (SMF) fault zones provide an opportunity to discuss several issues regarding damage zones and fault-rock development as a function of fault geometry, topology, and host-rock lithology. The PF is characterized by the classical geometry of a mature fault (e.g. Ben-Zion and Sammis, 2003), where strain has localized in a tabular, straight and continuous core of cataclastic material, and the surrounding damage zone appears to have already become largely passive in slip accommodation. In contrast, the SMF preserves the more complex structure of a still evolving fault zone, comprising both continuous rectilinear segments and a section characterized by complex contractional jogs. In addition, the development of the SMF through both quartzo-feldspathic (Tonalitic Lamella and Bressanone Granite) and phyllosilicate-rich rocks (Austroalpine phyllonites), allows direct comparison between the styles of deformation of these two lithologies.

In the following subsections, we discuss the environmental conditions during faulting and the different parameters influencing damage intensity and distribution. Lastly we draw some conclusions about the overall "maturity" of the PF and SMF fault zones and their basic scaling parameters.

6.1. Environmental conditions of faulting

The PF shows a relevant dextral and reverse offset, of the order of several to tens of kilometres. This results in a marked asymmetry between the northern hanging wall block (Austroalpine and Tonalitic Lamella), which was progressively exhumed from amphibolite-facies metamorphic conditions (Hoinkes et al., 1999) and the southern footwall block, which never underwent Alpine metamorphism. Instead, the younger SMF shows a reverse offset of less than 500 m (Fig. 8).

Our microstructural observations suggest a temperature of fault-rock formation in the 200–280 °C range on the basis of: (i) the lack of evidence of crystal plastic deformation of quartz ($T \leq 280$ °C; Stipp et al., 2002); (ii) the extensive precipitation of epidote both in the cataclasite matrix and in synkinematic veins (see discussion in Di Toro and Pennacchioni, 2004). In addition, the stability of epidote + quartz instead of laumontite + prehnite indicates $T > 200$–250 °C at 1–5 Kbar (Perkins et al., 1980). This temperature range, which is consistent with the base of the brittle crust, corresponds to depths of 7–11 km (assuming a geothermal gradient of 25–30 °C/km).

6.2. Lithologic control and mechanical anisotropy

Field and laboratory analyses of brittle faults in basement rocks have shown that the overall style of deformation and fracturing in damage zones is mainly controlled by lithology, depending on

whether the fault cuts through quartzo-feldspathic or phyllosilicate-rich host rocks. In the first case, deformation tends to localize in relatively thin (dm-scale) (ultra)cataclastic layers; in the second case a more distributed deformation within a wide fault zone (100 m–1 km-scale) is observed (e.g., Chester and Chester, 1998; Faulkner et al., 2003). On the other hand, geological and geophysical observations, as well as theoretical analysis, indicate that more extensive damage may be expected on the side of the fault where the stiffer material can be found, since this is characterized by faster seismic wave velocities and this leads to a preferred propagation direction for seismic waves released by earthquakes (e.g. Rubin, 2002; Dor et al., 2006, 2008; Lewis et al., 2007; Ampuero and Ben-Zion, 2008).

The contrast between wide damage zones observed within the Austroalpine phyllonitic paragneiss and the localized deformation in the Bressanone Granite fits the first model and is in agreement with what has been observed at the Carboneras fault (phyllosilicate-rich rocks; Faulkner et al., 2003) and the Punchbowl fault (quartzo-feldspathic rocks, Chester and Chester, 1998). According to Faulkner et al. (2003), this contrasting behaviour is ascribed to a supposed strain- and velocity-hardening behaviour of phyllosilicates within anastomosing (ultra) cataclasite layers in phyllosilicate-rich fault rocks. In our opinion, other factors may have played a role in the development of such a wide fault zone in phyllonitic paragneiss, such as the presence of a strong pre-existing planar fabric. It has been experimentally demonstrated that the anisotropy in shear strength due to a pre-existing planar fabric favors repeated failure along the foliation plane or at a low angle to it, with respect to failure at a high angle to the foliation (Paterson and Wong, 2005). In our opinion, both the wide damage zone in the Austroalpine basement and the relative weakness of the SMF ($\tau/\sigma_n = 0.27$; Fig. 7) result from the pervasive reactivation of the SCC' composite foliation in phyllonites. Enhanced damage and regional-scale weakness may be seen as two macroscopic effects of a micro-scale process: reactivation of the anisotropically weak inherited composite foliation. In any case, the "strengthening model" proposed by Faulkner et al. (2003), cannot be excluded on the basis of our data, and it is possible that both anisotropy and velocity-strengthening play a combined role.

6.3. Damage around the Leimgruben contractional jog

The 3D model clearly shows that one of the most important factors in determining deformation in damage zones, besides host-rock lithology, is the presence of a contractional jog, which represents an impediment to rigid-body displacement accumulation. The model efficiently highlights the fact that a lobe-shaped damage volume propagates to the NE in the Austroalpine Basement, in the extensional quadrant of the Leimgruben stepover. This is in general agreement with mechanical models and observations which predict the development of strong stress concentrations and diffuse inelastic deformation in the volume outside contractional jogs, propagating backward from the fault tip in the extensional quadrant (e.g. Segall and Pollard, 1980; Sibson, 1986), due to a coupled reduction in mean stress and increase in deviatoric stress that favors fracturing and faulting.

Partially in contrast with these models, the strong damage volume observed in the 3D model is not pinned directly to a fault tip, but higher DI values occur some hundreds of meters to the East, in a more "internal" position along the fault surface. This may be explained by considering the progressive evolution of the fault zone. Models of stress concentrations at tiplines are quasi-static (e.g. Segall and Pollard, 1980) and thus only depict the stress pattern at one infinitesimal strain increment, but the damage pattern reconstructed in our 3D model is the result of offset accumulation and fault propagation over geologic time. When we consider the tip line as the younger portion of a fault (which nucleated in some more internal sector), it is not surprising that more deformation accumulated in inner portions.

This strongly damaged lobe is likely to have a high vertical continuity. At least this is shown at the scale of our model (ca. 1.5 km in vertical direction). Although we did not find evidence for relevant fluid flow along the SMF (e.g. penetrative veining, hydrofracturing, etc.), either in the damage lobe or in other sectors, we may envisage that, in presence of, e.g. hydrothermal fluids, the damage lobe might have acted as a major conduit for enhanced sub-vertical fluid flow (e.g. Bonson et al., 2007).

6.4. Maturity and scaling parameters

Our results on scaling parameters may be compared with published compilations. The 0.075 D/L of the SMF corresponds to the upper range of data compilations (Childs et al., 2008) and this relatively high value may be explained by considering either: (i) the inferred weakness of the SMF, and/or (ii) that the western tip of the SMF is likely connected to the Brenner Detachment (hence, displacement does not vanish here).

The D/T and T/L of SMF are strongly influenced by the wide lobe-shaped damage volume associated with the Leimgruben contractional jog. In detail, the observation that the thickness of the damage zone around the Leimgruben contractional jog is one order of magnitude larger than that along rectilinear fault segments matches the statement by Sibson (1986), who emphasized that most "brecciation" occurs at jogs and particularly around contractional ones. This is related to the continuing accumulation of deformation due to kinematic incompatibility produced by the contractional jog, and this kind of deformation eventually ends only if the jog is breached (which is not the case for the SMF).

When we concentrate on the D/T values obtained for rectilinear segments, both SMF and PF values – 7.5 and >50 respectively – are approximately in agreement with the theoretical results of Cowie and Scholz (1992), who obtained values between 10 and 100, and with the field estimates of Vermilye and Scholz (1998). However, it is surprising to find a difference of one order of magnitude between D/T values obtained for faults developing in the same mechanical and environmental conditions and in the same rocks. In our opinion, the observation that the thickness of damage zones is the same along the rectilinear segments of both PF and SMF (ca. 200 m) means that this parameter is independent of the amount of displacement (1.5 km in the SMF vs. several km in the PF), and that the true significance of the D/T ratio should be re-evaluated (as already proposed by Childs et al., 2008). We propose two possible explanations for this observation, which deserve further investigations. A first hypothesis is that the thickness of damage zones along rectilinear fault segments (ca. 200 m) reflects the thickness of the process zones (Vermilye and Scholz, 1998), defined as the volume which undergoes fracturing during the initial stage of fault propagation and slip, and which is not related to any subsequent slip accumulation in the fault core. A second hypothesis is that damage may continue to accumulate during repeating slip events (e.g. Wilson et al., 2003), up to an equilibrium or saturation value (as in Mitchell and Faulkner, 2009), thus allowing for mature faults with very different offset to show almost the same damage zone thickness.

More generally, our observations indicate that damage zone thickness is more sensitive to the particular position in a fault array (rectilinear segment vs. jog) than to offset accumulation (1.5 km vs. tens of km for the SMF and PF, respectively). In fact, the progressive

refinement which results from slip accumulation tends to produce a smooth fault zone, where most asperities and geometrical irregularities (e.g. jogs) are removed. This process may result in the localization of the active slip zone within progressively thinner horizons, rather than in its thickening, as already evidenced by Childs et al. (2008).

6.5. Relationships between damage zones and fault rocks in core zones

Fault-rock and juxtaposition maps visualize symmetric and asymmetric core zones and show how elongate patches of probably different fault rocks can extend obliquely to the dip and slip vector. However, the boundaries of these patches, with an inferred strong rheological contrast, do not show any clear relationship with the DI parameter (Fig. 9). The lack of a correlation between inferred fault-rock type and damage zone thickness may appear to be at odds with some mechanical models and experimental data. In models (e.g. Dragoni, 1990), boundaries between patches with contrasting rheology are marked by stress concentrations (interpreted as asperities), which, in seismic data, may be interpreted as corresponding to clusters of aftershocks preferentially located along certain lithological contacts (as documented by Graymer et al., 2005, for the Hayward fault). We would like to emphasize that the different time-scale in these models and observations provides an explanation of this apparent paradox. Aftershocks, and earthquakes in general, occur on a short time-scale and in a quasi-static configuration in geologic terms, and, by definition, quasi-static mechanical models refer to a very short time-scale and static geometry. Conversely, our observations represent the cumulative effects of $>$1.5 km of offset developing along a considerable period of geologic time (at least some My). During this time, lithologic juxtaposition and fault-rock distributions continuously evolve with offset, so that stress concentrations developing at rheological boundaries along the fault zone migrate during their evolution according to complex and discontinuous patterns. If the wavelength of rheological boundaries is smaller than the total displacement (as in our case), the effect of each rheological boundary/stress concentration on damage development would be smoothed out over time. In other words, at each subsequent slip increment, a rheological boundary pinned to one fault block (e.g. hanging wall) exerts its influence on a different volume of the facing fault block (e.g. footwall), and the cumulative result of this process is a more homogeneous distribution of damage. For the same reason, a progressive “mixing” of fault rocks, dragged from different protoliths into core zones, may be envisaged. As a general consequence, structures in damage zones cannot be directly compared to quasi-static models and earthquake related damage, but must be confronted with evolutive models.

7. Conclusions

The Pusteria and Sprechenstein-Mules Fault Systems (PF and SMF) in the Italian Eastern Alps represent a natural laboratory to investigate damage distribution associated with faulting at the base of the seismogenic crust (8–10 km depth). Integration of 3-D modelling techniques with an ad-hoc classification of damage degree (the Damage Index, DI) enabled us to evaluate the relationships between damage zone, host rocks, and fault-rock distribution on a 10^4 m scale, thus bridging the gap between classical outcrop-scale description and large-scale geophysical models. Our main findings are summarized as follows.

1. Damage is more developed in phyllosilicate-rich foliated rocks (e.g. phyllonites) than in quartzo-feldspathic and massive rocks (e.g. granite). This is primarily ascribed to the pervasive cataclastic overprint along a pre-existing and favourably oriented phyllonitic composite fabric. The anisotropic weakness of this fabric may also provide a suitable explanation for the relative weakness and misorientation of the non-Andersonian SMF.
2. In general accord with other field observations and numerical models, the widest damage volume is associated with a major contractional jog (i.e. Leimgruben jog) and propagates in the extensional quadrant of the dextral SMF. The observation that the thickness of damage zones is almost the same along rectilinear segments of both PF and SMF (ca. 200 m) indicates that damage zone distribution is more sensitive to the particular position in a fault array (rectilinear segment vs. jog) than to offset accumulation (1.5 km vs. tens of km for the SMF and PF respectively).
3. The strong damage lobe associated with the Leimgruben contractional jog is not directly pinned to a fault tip, but occurs in a more internal position with respect to the inferred direction of fault segment propagation. This may be in contrast with the stress distribution described by quasi-static models, but may also be viewed as the result of long-term propagation and slip accumulation over geologic time.
4. Unlike the results from quasi-static models and observations of aftershock clustering, in our case there is no evidence of a direct relationship between damage distribution and the occurrence of different fault rocks along the main fault planes (DI vs. juxtaposition maps). This can be explained by the fact that the studied distribution of damage is the final stage of the long-term evolution of the faulting process, which accumulated (for the SMF) up to 1.5 km of offset over ca. 7 My.

Acknowledgments

This study was funded by the University of Padova (Progetto di Ateneo CPDA052291—Modellazione 3D dell’assetto geologico strutturale al margine occidentale della Finestra dei Tauri (Alpi Orientali)—2006/2007) and CARIPARO (Revealing the secrets of an earthquake: physico-chemical constraints from a multidisciplinary study of exhumed faults). BBT SE (the Italian–Austrian railway company in charge of the Brenner Basistunnel project) made available geophysical log data and borehole samples, and is gratefully acknowledged. The gOcad Research Group and Paradigm are acknowledged for welcoming the University of Padova into the gOcad Consortium (http://www.gocad.org). We thank Federico Zorzi for XRPD analysis and comments on results, students Claudio Pellegrini and Michele Fondriest for collecting some structural data, Giulio Di Toro and Giorgio Pennacchioni for useful discussions on fault rocks and mechanics, Andrea Zanchi for comments on regional tectonics, Simon Crowhurst and Gabriel Walton for the English revision. Ory Dor is acknowledged for very constructive comments to a first submission of this paper. Finally, we greatly appreciated the thorough and useful reviews by Steve Smith and Steven Hickman, and the editorial comments by Bob Holdsworth, which helped us to substantially improve the manuscript.

Appendix 1. Overview of geomodelling theory

We present here an outline of geomodelling techniques, based on the fundamental treatise by Mallet (2002), in order to show how, with the tools available in gOcad®, a rigorous computer model of the 3D architecture of a complex fault zone can be built, comprising linear, surface and volumetric geo-objects.

The basic assumption in geomodelling is that complex natural objects can be represented as (or approximated by) discrete models. In a discrete model, the topology of any object can be

approximated by a graph Ç(Ω,N), where Ω is the set of all the nodes of Ç, and N is an application from Ω to a subset N(α) of Ω, called the neighbourhood of α, so that N(α) contains the node α and all its surrounding nodes β_n (Fig. 8C). The graph Ç(Ω,N) does not take into account the properties of objects and is not sufficient to define topology unambiguously.

The discrete model M^n(Ω,N,φ,C) consists of the graph Ç(Ω,N) and of n functions $\varphi^n(\alpha)$, defined $\forall\ \alpha \in \Omega$, describing any property of the object. In practice, the first three components of $\varphi^n(\alpha)$, (e.g. $\varphi^x(\alpha)$, $\varphi^y(\alpha)$ and φ^z(i)), define the spatial coordinates, and the other components define any other property, including basic structural properties such as the attitude of a surface (defined as the gradient) and any other continuous or categorical property (e.g. degree of fracturing, porosity, seismic impedance, lithology, stratigraphic age, etc.). Hence, in this data-model, both the x, y, z coordinates and any other property are explicitly specified at the nodes of the discrete model and can be obtained by linear interpolation at any other point in the model space.

Property functions φ are controlled by a set C of linear constraints. C can be split into three subsets $C^{=}$, $C^{\approx}$ and $C^{>}$, comprising hard equality, soft equality and hard inequality constraints, respectively. $C^{=}$ are equality constraints that must be honoured strictly; $C^{\approx}$ are equality constraint that must be honoured in a least squares sense; $C^{>}$ are hard inequality constraints (soft inequality does not make sense). In practice, these constraints are defined according to available data, and property functions φ are simultaneously interpolated in order to honour all of them satisfactorily. The basic interpolation algorithm in the gOcad® package is DSI (Discrete Smooth Interpolator; Mallet, 2002), which was designed to interpolate φ by employing three criteria: (i) φ must be "as smooth as possible", (ii) hard constraints must be strictly honoured, (iii) soft constraints must be honoured "as much as possible". The relative weight of criteria (i) and (ii) can be adjusted, resulting in a more or less rough interpolation function. It is important to note that all the components of φ are interpolated simultaneously, so that constraints on spatial coordinates and their gradient (attitude), or porosity and seismic impedance, etc., can be strictly coupled with cross-constraints which must be honoured simultaneously.

The problem of defining unambiguous topology on Ç(Ω,N) is solved in gOcad® by means of cellular partition models based on GMaps, which provide a simple and rigorous framework for a topological/geometrical modelling environment (Lienhardt, 1994; Mallet, 2002). Readers are referred to Mallet (2002) for a detailed coverage of this topic, but we would like to describe here the most important points of this modelling approach.

- Biological organs, or organisms, are composed of sets of elementary cells. The overall arrangement – or structure – of cells determines the geometry and topology of an organ. The cellular partition paradigm uses this "template" as a tool to model natural objects with complex topology.
- GMaps provide the algebraic framework to model cellular partitions. In practice, embedded GMaps of increasing dimension are used, in order to model lines ($n = 1$), surfaces ($n = 2$) and solids ($n = 3$) in R^3. The algebraic structure of GMaps permits the definition of a set of operators to create or edit (delete, cut, sew, merge, etc.) cellular partitions, which automatically honour topology, avoiding geometrical inconsistencies at any stage of the modelling workflow.

The practical problem of subdividing the space in a cellular representation is addressed in gOcad by different tessellation algorithms. Delaunay tessellation (for surfaces or solids) is useful when data points are fairly well distributed in 3D and surfaces are not too complex (e.g. tight or refolded folds cannot be modelled with this algorithm). Other algorithms are useful when building triangulated surfaces defined by their bordering curves, or when decomposing a solid based on regular (hexahedral), curved or unstructured (tetrahedral) grids. The final result of such tessellation algorithms is a draft model, with correct topology and approximate geometry, which can later be refined by interpolation in order to honour all available constraints. For instance, a fault surface can be first generated, with a tessellation algorithm, from its trace (intersection with topographic surface) and later refined by DSI interpolation, in order to honour all available data, i.e. outcrop and borehole location and attitude data.

Appendix 2. Handling surface geological data in a 3D modelling workflow

In this appendix we describe the procedure followed in order to generate fault surfaces starting from field and borehole data in the gOcad® model.

1. A geographic information system (GIS) was implemented, in which all relevant field geological and structural data were stored. Spatial data (outcrops, fault traces, structural stations, etc.) were georeferenced in 2D with a GPS, to an accuracy of 5 m or better. Elevation data were retrieved from a high-resolution digital elevation model derived from an aerial LIDAR survey (2.5 × 2.5 m grid).
2. Data from the GIS and boreholes were imported into gOcad® via customized routines (Bistacchi et al., 2008), retaining 3D georeferencing and all relevant attributes. The most valuable borehole data for this model are stratigraphy, comprising detailed characterization of fault rocks performed on continuous cores, and fracture data, based on BHTV data cross-checked with continuous cores. Borehole data were recorded in measured depth (MD) and then converted into the rectilinear gOcad® coordinate system (x, y, z) using wellhead location and borehole directional surveys. These directional surveys were also used to correct apparent strike and dip of fractures in the BHTV logs to true strike and dip.
3. A draft model was reconstructed by simply extruding fault traces along-dip. The topology of the fault network, including intersection relationships and the hierarchy of faults and between faults and geological boundaries, was checked and corrected at this stage.
4. A set of structural constraints was imposed on fault surfaces (see Appendix 1): "hard" control nodes where a given fault was actually observed, "soft" control points where a fault is presumed to be identified with a given accuracy, attitude control points where attitude is known, and intersection constraints at the intersection between two faults or between a fault and a geological boundary (in this way, intersections remain "sealed" during the interpolation and fault network topology is preserved).
5. The Discrete Smooth Interpolation (DSI; Mallet, 2002) algorithm was run on the assembled data. The balance between local roughness and conformity to soft constraints was controlled by means of weighting factors associated with constraints, in order to obtain the most realistic fault surfaces (see Appendix 1).

Surfaces reconstructed with this methodology weigh field data according to their quality (hard or soft constraints) and retain the topology imposed in the draft model (Fig. 8).

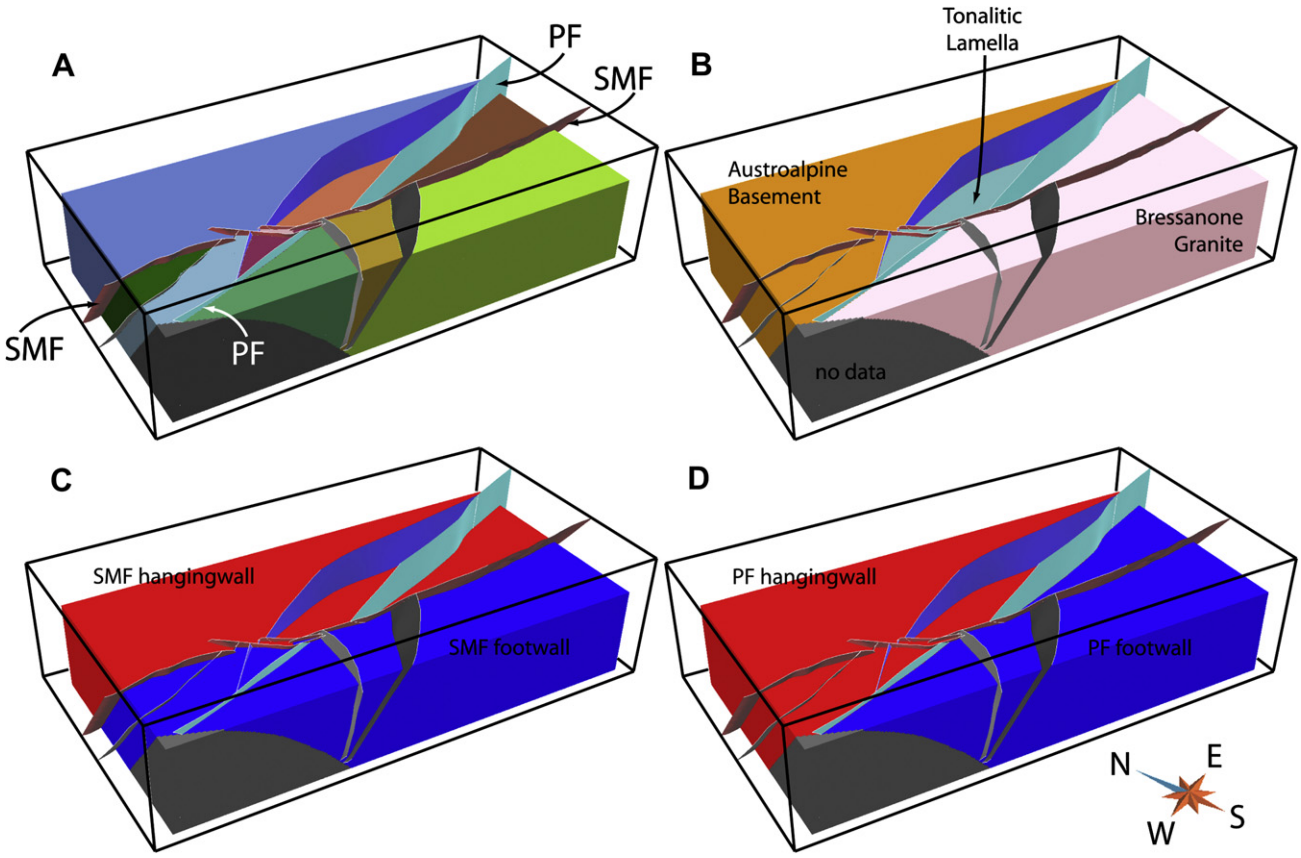

Fig. 10. (A) Fault network (PF: Pusteria Fault; SMF: Sprechenstein-Mules Fault), northern boundary of Tonalitic Lamella and "fault blocks" (color coded) as defined in 3D modelling subsection; (B) fault network and fault blocks classified as tectonic units (same color legend as in Fig. 1); (C) fault network and fault blocks classified as hanging wall/footwall (red/blue) of PF; (D) fault network and fault blocks classified as hanging wall/footwall (red/blue) of the SMF. View from SW. 3D solid model is 8 × 4 × 1.5 km. (For interpretation of the references to color in this figure legend, the reader is referred to the web version of this article.)

Appendix 3. Construction of fault surface and juxtaposition maps

In this appendix we describe the procedure followed in order to generate fault surface and juxtaposition maps in the gOcad® model. This procedure can be subdivided in five steps:

1. Distinguishing volumes separated by faults, defined as "fault blocks" (the model is composed of 12 fault blocks; Fig. 10);
2. For each fault block, defining whether it belongs to the hanging wall or to the footwall of the major faults (PF or SMF; Fig. 10);
3. Identifying, for each fault block, the tectonic unit to which it belongs (Fig. 10);
4. Computing the intersection of classified fault blocks with fault surfaces, thus limiting patches of fault surfaces which are in contact with a single fault block (e.g. "patch A of SMF is in contact with Tonalitic Lamella"): this process must be run twice, first for the hanging wall and then for the footwall, and results in two fault-surface geological maps, one for the hanging wall and the other for the footwall;
5. calculating the intersection between the fault-surface geological maps of the hanging wall and footwall to obtain the juxtaposition map (Fig. 9).

Appendix 4. Evaluation of uncertainty in the 3D model

The level of uncertainty in 3D reconstructions is heterogeneous and may be estimated by means of the techniques discussed in Bistacchi et al. (2008). In summary, uncertainty is smallest close to data points (outcrops or boreholes) and increases with distance from them, with gradients that vary depending on each particular structure and parameter. For instance, uncertainty in position for a planar fault (e.g. planar segments of PF and SMF), which can be continuously observed along trace for some kilometres and along-dip for a thousand meters (thanks to rugged Alpine topography), is limited and increases linearly with distance from data points (outcrops and boreholes). Uncertainty may be higher in complex sectors, such as stepovers, but in this study we could rely on $>$ 2000 m of continuous coring boreholes and geophysical logs, which considerably lowered uncertainty in the Leimgruben stepover.

It was more difficult to define uncertainty in volumetric parameters, such as DI. In order to control volumetric uncertainties we: (i) performed some tests by splitting the dataset and using part of it for a-posteriori checks on interpolation, which gave good results, and (ii) based our entire discussion on sections across the 3D model which were more or less in the centroid of our dataset, where data are more continuous and interpolation more coherent. In conclusion, although some uncertainty is implied in such a regional-scale model, spatial uncertainty is generally considered smaller than the model resolution (25 × 25 × 20 m/voxet) and does not affect the overall interpretation.

Appendix. Supplementary material

Supplementary material can be found, in the online version, at doi:10.1016/j.jsg.2010.06.003.

References

Ampuero, J.-P., Ben-Zion, Y., 2008. Cracks, pulses and macroscopic asymmetry of dynamic rupture on a biomaterial interface with velocity-weakening friction. Geophysical Journal International 173, 674–692.

Anderson, E.M., 1951. Dynamics of Faulting and Dyke Formations with Application to Britain. Oliver & Boy, Edinburgh.

Angelier, J., 1990. Inversion of field data in fault tectonics to obtain the regional stress. III. A new rapid direct inversion method by analytical means. Geophysical Journal International 103, 363–376.

Antonellini, M., Aydin, A., 1995. Effect of faulting on fluid flow in porous sandstones: geometry and spatial distribution. AAPG Bulletin 79, 642–671.

Baggio, P., Borsellini, A., et al., 1969. Carta Geologica D'Italia 1:100.000, Foglio 1-4, Passo del Brennero-Bressanone, con Note Illustrative. Servizio Geologico d'Italia.

Barth, S., Oberli, F., Meier, M., 1989. U–Th–Pb systematics of morphologically characterized zircon and allanite: a high-resolution isotopic study of the Alpine Rensen pluton (northern Italy). Earth and Planetary Science Letters 95, 235–254.

Ben-Zion, Y., Sammis, C., 2003. Characterization of fault zones. Pure and Applied Geophysics 160, 677–715.

Berg, S.S., Skar, T., 2005. Controls on damage zone asymmetry of a normal fault zone: outcrop analyses of a segment of the Moab fault, SE Utah. Journal of Structural Geology 27, 1803–1822.

Bigi, G., Cosentino, D., Parotto, M., Sartori, R., Scandone, P., 1990. Structural model of Italy, Sheet no. 1. In: Castellarin, A., Coli, M., Dal Piaz, G.V., Sartori, R., Scandone, P., Vai, G.B. (Eds.), Structural Model of Italy, Progetto Finalizzato Geodinamica. CNR, Rome.

Billi, A., Salvini, F., Storti, F., 2003. The damage zone-fault core transition in carbonate rocks: implications for fault growth, structure and permeability. Journal of Structural Geology 25, 1779–1794.

Bistacchi, A., Dal Piaz, G.V., Dal Piaz, G., Massironi, M., Monopoli, B., Schiavo, A., 2003. Carta Geologica e note illustrative del transetto Val di Vizze-Fortezza (Alpi Orientali). Memorie di Scienze Geologiche di Padova 55, 169–189.

Bistacchi, A., Massironi, M., Dal Piaz, G.V., Dal Piaz, G., Monopoli, B., Schiavo, A., Toffolon, G., 2008. 3D fold and fault reconstruction with uncertainty model: an example from an Alpine tunnel case study. Computers and Geosciences 34, 351–372.

Bonson, C.G., Childs, C., Walsh, J.J., Schöpfer, M.P.J., Carboni, V., 2007. Geometric and kinematic controls on the internal structure of a large normal fault in massive limestones: the Maghlaq Fault, Malta. Journal of Structural Geology 29, 336–354.

Borsi, S., Del Moro, A., Sassi, F.P., Zirpoli, G., 1978. On the age of the Periadriatic Rensen massif (Eastern Alps). Neues Jahrbuch für Geologie und Paläontologie Monatshefte 5, 262–272.

Bürgi, C., Parriaux, A., Franciosi, G., Rey, J-Ph, 1999. Cataclastic rocks in underground structures-terminology and impact on the feasibility of projects (initial results). Engineering Geology 51, 225–235.

Caine, J.S., Evans, J.P., Forster, C.B., 1996. Fault zone architecture and permeability structure. Geology 24, 1025–1028.

Carena, S., Suppe, J., 2002. Three-dimensional imaging of active structures using earthquake aftershocks: the Northridge thrust, California. Journal of Structural Geology 24, 887–904.

Chester, F.M., Chester, J.S., 1998. Ultracataclasite structure and friction processes of the Punchbowl fault, San Andreas system, California. Tectonophysics 295, 199–221.

Chester, F.M., Evans, J.P., Biegel, R.L., 1993. Internal structure and weakening mechanisms of the San Andreas fault. Journal Geophysical Research 98, 771–786.

Chester, F.M., Logan, J.M., 1986. Implications for mechanical properties of brittle faults from observations of the Punchbowl fault zone, California. Pure and Applied Geophysics 124, 79–106.

Childs, C., Manzocchi, T., Walsh, J.J., Bonson, C.G., Nicol, A., Schöpfer, M.P.J., 2008. A geometric model of fault zone and fault rock thickness variations. Journal of Structural Geology 31 (2), 117–127.

Collettini, C., Holdsworth, R.E., 2004. Fault zone weakening and character of slip along low-angle normal faults: insights from the Zuccale Fault, Elba, Italy. Journal of the Geological Society of London 161, 1039–1051.

Cowie, P.A., Scholz, C.H., 1992. Growth of faults by accumulation of seismic slip. Journal of Geophysical Research 97 (B7), 11.085–11.095.

Dal Piaz, G.V., Bistacchi, A., Massironi, M., 2003. Geological outline of the Alps. Episodes 26 (3), 175–180.

Dershowitz, W.S., Herda, H., 1992. Interpretation of fracture spacing and intensity. In: Proceedings of the 33rd U.S. Symposium on Rock Mechanics, Santa Fe, N. Mexico. A.A. Balkema, Rotterdam, pp. 757–766.

Di Toro, G., Pennacchioni, G., 2004. Superheated friction-induced melts in zoned pseudotachylytes within the Adamello tonalites (Italian Southern Alps). Journal of Structural Geology 26, 1783–1801.

Di Toro, G., Pennacchioni, G., 2005. Fault plane processes and mesoscopic structure of a strong-type seismogenic fault in tonalites (Adamello batholith, Southern Alps). Tectonophysics 402, 54–79.

Dor, O., Rockwell, T.K., Ben-Zion, Y., 2006. Geological observations of damage asymmetry in the structure of the San Jacinto, San Andreas and Punchbowl faults in the Southern California: a possible indicator for preferred rupture propagation direction. Pure and Applied Geophysics 163, 301–349.

Dor, O., Yildirim, C., Rockwell, T.K., Ben-Zion, Y., Emre, O., Sisk, M., Duman, T.Y., 2008. Geological and geomorphologic asymmetry across the rupture zones of the 1943 and 1944 earthquakes on the North Anatolian Fault: possible signals for preferred earthquake propagation direction. Geophysical Journal International 173, 483–504.

Dragoni, M., 1990. A model of interseismic fault slip in the presence of asperities. Geophysical Journal International 101, 147–156.

Faulkner, D.R., Lewis, A.C., Rutter, E.H., 2003. On the internal structure and mechanics of large strike-slip fault zones: field observations of the Carboneras fault in southeastern Spain. Tectonophysics 367, 235–251.

Fodor, L., Jelen, B., Márton, E., Skaberne, D., Čar, J., Vrabec, M., 1998. Miocene–Pliocene tectonic evolution of the Slovenian Periadriatic fault: implications for the Alpine-Carpathian models. Tectonics 17, 690–709.

Francese, R., Mazzarini, F., Bistacchi, A., Morelli, G., Pasquarè, G., Praticelli, N., Robain, H., Wardell, N., Zaja, A., 2009. Structural and geophysical approach to the study of fractured Reservoirs in the Scansano-Magliano in Toscana Ridge, southern Tuscany, Italy. Hydrogeology Journal. doi:10.1007/s10040-009-0435-1.

Frisch, W., Dunkl, I., Kuhlemann, J., 2000. Postcollisional orogen-parallel large-scale extension in the Eastern Alps. Tectonophysics 327, 239–265.

Fügenschuh, B., Seward, D., Mancktelow, N., 1997. Exhumation in a convergent orogen: the western Tauern window. Terra Nova 9, 213–217.

Graymer, R.W., Ponce, D.A., Jachens, R.C., Simpson, R.W., Phelps, G.A., Wentworth, C.M., 2005. Three-dimensional geologic map of the Hayward fault, northern California: correlation of rock units with variations in seismicity, creep rate, and fault dip. Geology 33, 521–524.

Heitzmann, P., 1985. Kakirite, Kataklasite, Mylonite-Zur Nomenklatur der Metamorphite mit Verformungsgefüge. Eclogae Geologicae Helvetiae 78, 273–286.

Hoek, E., 1994. Strength of rock and rock masses. ISRM News Journal 2 (2), 4–16.

Hoek, E., Brown, E.T., 1997. Practical estimation of rock mass strength. International Journal of Rock Mechanics and Mining Sciences 34 (8), 1165–1186.

Hoek, E., Marinos, P., Benissi, M., 1998. Applicability of the Geological Strength Index (GSI) classification for very weak and sheared rock masses. The case of the Athens Schist Formation. Bulletin of Engineering Geology and the Environment 57 (2), 151–160.

Hoinkes, G., Koller, F., Rantitsch, G., Dachs, E., Höck, V., Neubauer, F., Schuster, R., 1999. Alpine metamorphism of the eastern Alps. Schweizerische Mineralogische und Petrographische Mitteilungen 79, 155–181.

Jefferies, S.P., Holdsworth, R.E., Shimamoto, T., Takagi, H., Lloyd, G.E., Spiers, C.J., 2006. Origin and mechanical significance of foliated cataclastic rocks in the cores of crustal-scale faults: examples from the Median Tectonic line, Japan. Journal of Geophysical Research 111, B12303. doi:10.1029/2005JB004205.

Kurtz, W., Neubauer, F., Genser, J., Dachs, E., 1998. Alpine geodynamic evolution of passive and active continental margin sequences in the Tauern window (eastern Alps, Austria, Italy): a review. Geologische Rundschau 87, 225–242.

Lewis, M.A., Peng, Z., Ben-Zion, Y., Vernon, F.L., 2005. Shallow seismic trapping structure in the San Jacinto fault zone near Anza, California. Geophysical Journal International 162, 867–881.

Lewis, M.A., Ben-Zion, Y., McGuire, J., 2007. Imaging the deep structure of the San Andreas Fault south of Hollister with joint analysis of fault zone head and direct P arrivals. Geophysical Journal International 169, 1028–1042.

Li, Y.-G., Leary, P.C., 1990. Fault zone trapped waves. Bulletin of the Seismological Society of America 80, 1245–1271.

Lienhardt, P., 1994. N-dimensional generalized combinatorial maps and cellular quasi-manifolds. International Journal of Computational Geometry and Applications 4 (3), 275–324.

Mallet, J.L., 2002. Geomodeling. Oxford University Press, New York.

Mancktelow, N., Stöckli, D.F., Grollimund, B., Müller, W., Fügenschuh, B., Viola, G., Seward, D., Villa, I.M., 2001. The DAV and Periadriatic fault system in the Eastern Alps south of the Tauern window. International Journal of Earth Sciences 90, 593–622.

Martì, D., Carbonell, R., Tryggvason, A., Escuder, J., Pérez-Estaùn, A., 2002. Mapping brittle fracture zones in three dimensions: high resolution travel time seismic tomography in a granitic pluton. Geophysical Journal International 149, 95–105.

Micarelli, L., Moretti, I., Jaubert, M., Moulouel, H., 2006. Fracture analysis in the south-western Corinth rift (Greece) and implications on fault hydraulic behavior. Tectonophysics 426, 31–59.

Mitchell, T.M., Faulkner, D.R., 2009. The nature and origin of off-fault damage surrounding strike-slip fault zones with a wide range of displacements: a field study from the Atacama fault system, northern Chile. Journal of Structural Geology 31, 802–816.

Müller, W., Prosser, G., Mancktelow, N., Villa, I.M., Kelley, P.S., Viola, G., Oberli, F., 2001. Geochronological constraints on the evolution of the Periadriatic fault system (Alps). International Journal of Earth Sciences 90 (3), 623–653.

Paterson, M.S., Wong, T.-F., 2005. Experimental Rock Deformation – The Brittle Field, second ed. Springer-Verlag, Berlin, Heidelberg.

Perkins, D., Westrum, E.F., Essene, E.J., 1980. The thermodynamic properties and phase relations of some minerals on the system $CaO–Al_2O_3–SiO_2–H_2O$. Geochimica et Cosmochimica Acta 44, 61–84.

Petit, J.P., 1987. Criteria for the sense of movement on fault surfaces in brittle rocks. Journal of Structural Geology 9, 597–608.

Pollard, D.D., Fletcher, R.C., 2005. Fundamentals of Structural Geology. Cambridge University Press, Cambridge.

Ratschbacher, L.W., Frisch, H., Linzer, G., Merle, O., 1991. Lateral extrusion in the eastern Alps, Part 2: structural analysis. Tectonics 10, 257–271.

Ritter, O., Hoffmann-Rothe, A., Bedrosian, P.A., Weckmann, U., Haak, V., 2005. Electrical conductivity images of active and fossil fault zones. In: Bruhn, D.,

Burlini, L. (Eds.), High-strain Zones: Structure and Physical Properties, vol. 245. Geological Society of London Special Publication, pp. 165–186.
Rubin, A., 2002. Aftershocks of microearthquakes as probes of the mechanics of rupture. Journal Geophysical Research 107. doi:10.1029/2001JB0000496.
Rutter, E.H., Holdsworth, R.E., Knipe, R.J., 2001. The nature and tectonic significance of fault-zone weakening: an introduction, vol. 186. Geological Society of London Special Publication. 1–11.
Schmid, S.M., Aebli, H.R., Zingg, A., 1989. In: Coward, M.P., Dietrich, D., Park, R.G. (Eds.), The role of the Periadriatic Line in the tectonic evolution of the Alps, vol. 45. Geological Society of London Special Publication, Alpine Tectonics, pp. 153–171.
Schmid, S.M., Pfiffner, O.A., Schönborn, G., Froitzheim, N., Kissling, E., 1997. Integrated Cross-section and Tectonic Evolution of the Alps along the Eastern Traverse. In: Pfiffner, O.A., Lehner, P., Heitzman, P., Mueller, S., Steck, A. (Eds.), Deep Structure of the Swiss Alps. Birkhäuser, Basel, pp. 289–304.
Scholz, C.H., 2002. The Mechanics of Earthquakes and Faulting, second ed. Cambridge University Press, Cambridge.
Segall, P., Pollard, D.D., 1980. Mechanics of discontinuous faults. Journal of Geophysical Research 85, 4337–4350.
Selverstone, J., 1988. Evidence for east–west crustal extension in the Eastern Alps: implications for the unroofing history of the Tauern window. Tectonics 7, 87–105.
Selverstone, J., 2005. Are the Alps Collapsing? Annual Review of Earth and Planetary Sciences 33, 113–132.
Sibson, R.H., 1977. Fault rocks and fault mechanisms. Journal of the Geological Society 133 (3), 191–213.
Sibson, R.H., 1986. Brecciation processes in fault zones: inferences from earthquake Rupturing. Pure and Applied Geophysics 124, 159–175.
Spang, J.H., 1972. Numerical method for dynamic analysis of calcite Twin Lamellae. Geological Society of America Bulletin 83 (1), 467–472.
Stipp, M., Stünitz, H., Heilbronner, R., Schmid, S.M., 2002. The eastern Tonale fault zone: a "natural laboratory" for crystal plastic deformation of quartz over a temperature range from 250 to 700°C. Journal of Structural Geology 24, 1861–1884.
Transalp Working Group, 2002. First deep seismic images of the Eastern Alps reveal giant crustal wedges. Geophysical Research Letters 29, 10.1029–10.1032.
Tzamos, S., Sofianos, A.I., 2007. A correlation of four rock mass classification systems through their fabric indices. International Journal of Rock Mechanics and Mining Sciences 44, 477–495.
Unsworth, M.J., Malin, P.E., Egbert, G.D., Booker, J.R., 1997. Internal structure of the San Andreas fault at Parkfield, California. Geology 25 (4), 359–362.
Vermilye, J.M., Scholz, C.H., 1998. The process zone: a microstructural view of fault growth. Journal of Geophysical Research 103, 12.223–12.237.
Wilson, J.E., Chester, J.S., Chester, F.M., 2003. Microfracture analysis of fault growth and wear processes, Punchbowl Fault, San Andreas system, California. Journal of Structural Geology 25, 1855–1873.
Zwingmann, H., Mancktelow, N., 2004. Timing of Alpine fault gouges. Earth and Planetary Science Letters 223, 415–416.